Towards Bio-compatible Magnetic Nanoparticles: Immune-related Effects, *In-vitro* Internalization, and *In-vivo* Bio-distribution of Zwitterionic Ferrite Nanoparticles with Unexpected Renal Clearance

Anna M. Ferretti,[a#] Sandro Usseglio,[a#] Sara Mondini,[a] Carmelo Drago,[b] Rosa La Mattina,[b] Bice Chini,[c] Claudia Verderio,[c] Marianna Leonzino,[c] Cinzia Cagnoli,[c] Pooja Joshi,[c] Diana Boraschi,[d] Paola Italiani,[d] Yang Li,[d§] Benjamin J. Swartzwelter,[d] Luigi Sironi,[e,f] Paolo Gelosa,[e,f] Laura Castiglioni,[e] Uliano Guerrini,[g] Alessandro Ponti [*,a]

[a] Istituto di Scienze e Tecnologie Chimiche "Giulio Natta" (SCITEC), Consiglio Nazionale delle Ricerche, Via G. Fantoli 16/15, 20138 Milano, Italy

[b] Istituto di Chimica Biomolecolare (ICB), Consiglio Nazionale delle Ricerche. Via P. Gaifami, 18, 95126 Catania, Italy.

[c] Istituto di Neuroscienze (IN), Consiglio Nazionale delle Ricerche, Via L. Vanvitelli 32, 20129 Milano, Italy.

[d] Istituto di Biochimica e Biologia Cellulare (IBBC), Consiglio Nazionale delle Ricerche, Via P. Castellino 111, 80131 Napoli, Italy.

[e] Dipartimento di Scienze Farmaceutiche, Università degli Studi di Milano, Via G. Balzaretti 9, 20133 Milano, Italy.

[f] Centro Cardiologico Monzino IRCCS, Via C. Parea 3, 20138 Milano, Italy.

[g] Dipartimento di Scienze Farmacologiche e Biomolecolari, Università degli Studi di Milano, Via G. Balzaretti 9, 20133 Milano, Italy.

[#] These authors contributed equally to the work.

[§] Present address: Institute of Biomedicine and Biotechnology, Shenzhen Institutes of Advanced Technology, Chinese Academy of Sciences, Shenzhen, China.

[*] Corresponding Author

Alessandro Ponti

Istituto di Scienze e Tecnologie Chimiche "Giulio Natta" (SCITEC), Consiglio Nazionale delle Ricerche, Via G. Fantoli 16/15, 20138 Milano, Italy

E-mail: alessandro.ponti@scitec.cnr.it.

Phone: +39 02 5031 4280. Fax: +39 02 5031 3927.

Abstract

Hypothesis. Iron oxide and other ferrite nanoparticles have not yet found widespread application in the medical field since the translation process faces several big hurdles. The incomplete knowledge of the interactions between nanoparticles and living organisms is an unfavorable factor. This complex subject should be made simpler by synthesizing magnetic nanoparticles with good physical (relaxivity) and chemical (colloidal stability, anti-fouling) properties and no biological activity (no immune-related effects, minimal internalization, fast clearance). Such an innocent scaffold is the main aim of the present paper. We systematically searched for it within the class of small-to-medium size ferrite nanoparticles coated by small (zwitter)ionic ligands. Once established, it can be functionalized to achieve targeting, drug delivery, etc. and the observed biological effects will be traced back to the functional molecules only, as the nanosized scaffold is innocent.

Experiments. We synthesized nine types of magnetic nanoparticles by systematic variation of core composition, size, coating. We investigated their physico-chemical properties and interaction with serum proteins, phagocytic microglial cells, and a human model of inflammation and studied their biodistribution and clearance in healthy mice. The nanoparticles have good magnetic properties and their surface charge is determined by the preferential adsorption of anions. All nanoparticle types can be considered as immunologically safe, an indispensable pre-requisite for medical applications in humans. All but one type display low internalization by microglial BV2 cells, a process strongly affected by the nanoparticle size. Both small (3 nm) and medium size (11 nm) zwitterionic nanoparticles are in part captured by the mononuclear phagocyte system (liver and spleen) and in part rapidly (≈1 h) excreted through the urinary system of mice.

Findings. The latter result questions the universality of the accepted size threshold for the renal clearance of nanoparticles (5.5 nm). We suggest that it depends on the nature of the circulating particles. Renal filterability of medium-size magnetic nanoparticles is appealing because they share with small nanoparticles the decreased accumulation-related toxicity while performing better as magnetic diagnostic/therapeutic agents thanks to their larger magnetic moment. In conclusion, many of our nanoparticle types are a bio-compatible innocent scaffold with unexpectedly favorable clearance.

Keywords. Zwitterionic nanoparticles; magnetic nanoparticles; immune-related effects; internalization; microglia; bio-distribution; renal clearance.

1. Introduction

Translating magnetic nanoparticles (NPs) into clinical practice has proved a difficult process. In 2018, just five magnetic NP formulations indicated for iron replacement therapy were FDA- and EMA-approved and marketed while the previously approved magnetic NP contrast agents have been withdrawn from the market.[1-5] A few successful examples can be found in the device category, such as Nanotherm (MagForce AG) for hyperthermia treatment of glioblastoma and the recently approved Magtrace/Sentimag (Endomagnetics Ltd.) to guide lymph node biopsies.[6]

Several hurdles limit the clinical translation and marketability of NPs.[7] For instance, only a minor fraction (≤0.7%) of intravenously injected inorganic NPs (Au or SiO_2) with a cancer-targeting coating (Trastuzumab or folic acid) reach the tumor site and just 0.002% of these actually enter cancerous cells.[8] The most important hurdles are the complexity of NP-based diagnostic/therapeutic systems, incomplete understanding of the interaction of NPs with living organisms (especially the NP pharmaco-kinetics and -dynamics), immunological effects (immuno-stimulation, -suppression, -toxicity),[3-5] and the accumulation of NPs in organs, often related to the effective scavenger action of the mononuclear phagocyte system (MPS).[9].

To reduce the structural complexity that makes it difficult to optimize NPs with regard to the many requirements needed for a successful translation into clinical practice, we focus on a simpler NP structure, as recommended in Ref. [5]. We aim at establishing a bio-compatible magnetic NP scaffold, comprising an inorganic magnetic crystalline core coated with a small organic ligand (as opposed to polymeric ligands). The scaffold should have weak interaction with the organism, leading to low protein adsorption and non-specific cell internalization, absence of immune-related effects, and favorable bio-distribution and clearance. Such an innocent scaffold would be available for grafting with a biologically-functional ligand (*e.g.*, a targeting or diagnostic or therapeutic molecule) and the investigation of this functional NP-based system would be easier since we will know that the magnetic NP scaffold itself is innocent.

Magnetic NPs have already been reported in the literature as bio-compatible, mostly based on their low protein adsorption, cellular uptake, and cytotoxicity. [10-12] On the other hand, most magnetic NPs display immune-related effects. [3] We systematically searched for the desired magnetic NP scaffold within the class of spherical, small-to-medium size, spinel ferrite NPs coated by short-chain (zwitter)ionic ligands. Spinel ferrites MFe_2O_4 are a class of magnetic oxides, widely used because of their good bio-compatibility and efficacy as an agent for magnetic resonance imaging (MRI), hyperthermia, and magnetic drug delivery.[13] Small

ionic or zwitterionic ligands have recently received much attention because of their ability to reduce protein adsorption [14-16] and because zwitterion-coated NPs exhibit low association with immune cells in whole human blood. [17]

In 2007 zwitterionic sulfobetaine-coated Au NPs [18] and carboxybetaine-coated (cysteine) quantum dots [19] were reported. The latter study established the size threshold for the renal clearance of NPs at 5.5 nm. Later, several quantum dots and gold NPs coated with carboxy- or sulfo-betaines displayed minimal protein adsorption and low aspecific internalization; only small zwitterions provided the NPs with favorable clearance. [15] Two examples of magnetic iron oxide NPs were reported: NPs coated with a carboxybetaine polyampholyte [20] or the small zwitterionic dopamine sulfonate (ZDS) molecule. [21] The latter NPs have low affinity toward serum proteins both *in vitro* and *in vivo* (mice) are scarcely taken up by HeLa [22] and HepG2 cells. [23] Immune-related effects were investigated only for iron oxide NPs coated with two polymeric carboxybetaines. NPs coated with 3-(dimethylamino)propylamine-substituted poly(maleic anhydride-*alt*-1-decene) did not induce a change in cytokine or chemokine levels [24] whereas NPs coated with distearoylphosphoethanolamine-polycarboxybetaine (DSPE-PCB) induced a strong mixed Th1/Th2 type immune response but did not change the IL-10 level. [25] In both cases, NPs were *not* tested for bacterial endotoxin.

We selected two zwitterionic ligands, dopamine sulfonate (DS) and ZDS, [21] in addition to caffeic acid (CAF) and coryneine chloride (COR), which provide nominally anionic and cationic coating, respectively (Figure 1). We chose a diameter range (3 to 22 nm) that spans from ultrasmall to medium-size and corresponds to two orders of magnitude change for volume and magnetic moment.[26]. This size range can be accessed by thermal-decomposition synthetic methods, which yields monodisperse crystalline NPs and it is below the 50-200 nm range that elicits highly effective scavenging from the MPS. [27]

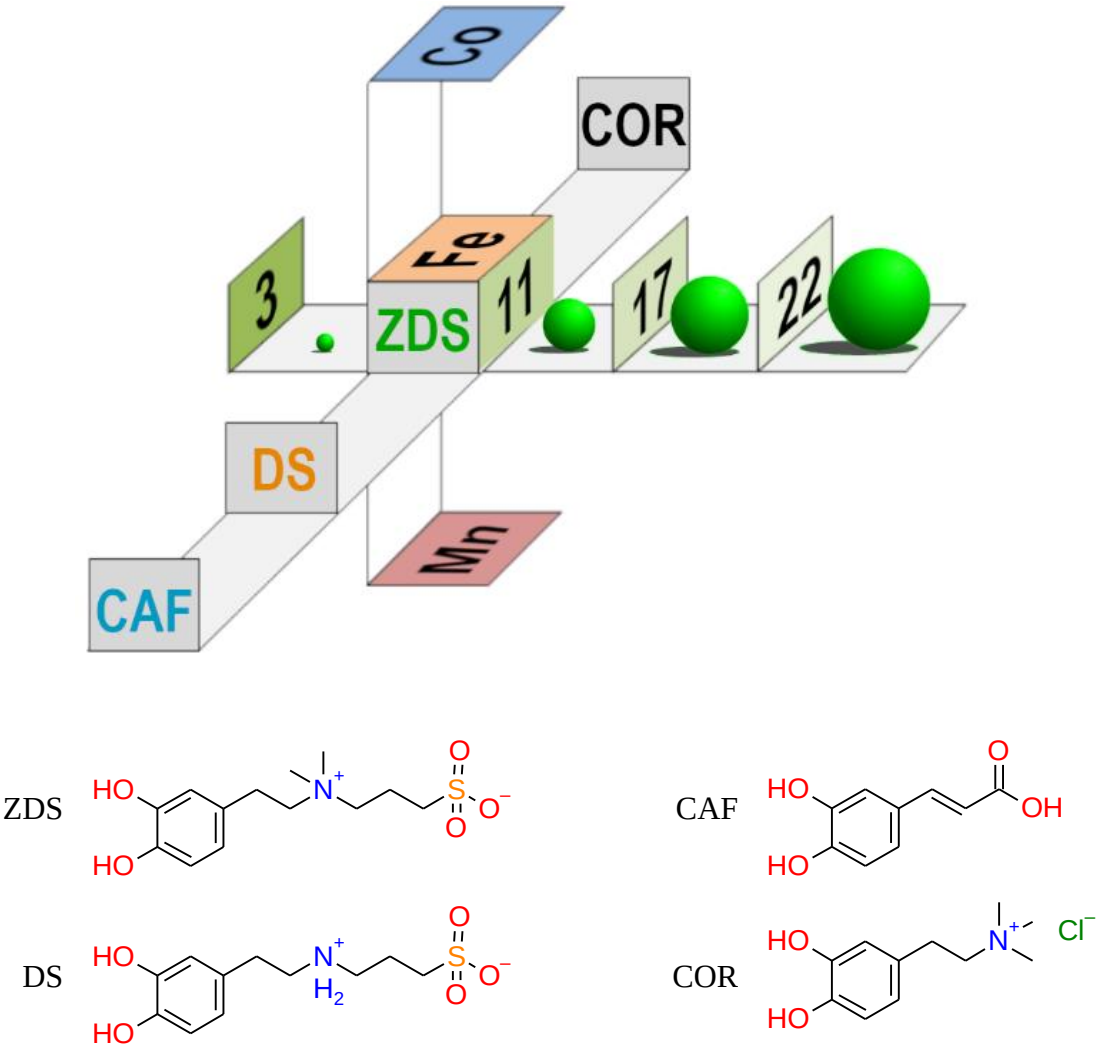

Figure 1. Pictorial representation of the systematic one-factor-at-a-time variation of the physico-chemical properties of the ferrite NPs used in this study. The horizontal axis represents the NP mean diameter (3 to 22 nm), the vertical axis portrays the divalent atom present in the ferrite core (Mn, Fe, Co), and the front-back axis depicts the (zwitter)ionic ligands. Their chemical structure is shown.

In addition to the physico-chemical characterization of the NPs, we investigated immune-related effects, cellular internalization, and bio-distribution. The former are of utmost importance because, on one hand, NP-based drugs and devices inducing immune-mediated adverse effects [3-5, 28, 29] are unlikely to be successfully translated but, on the other hand, they can improve the promising anticancer immunotherapies by modulating the behavior of myeloid and lymphoid cells.[30] Immune-related effects were studied by a whole human blood

assay and an *in vitro* kinetic model of inflammation based on primary human monocytes. Aimed at minimizing non-specific internalization, we assessed cellular internalization using highly phagocytic immortalized murine microglial cell line BV2. BV2 cells can also provide useful information about the fate of NPs present in the central nervous system (CNS) since t cells appear to be a valid substitute for primary microglia in many experimental settings. [31] Furthermore, prompted by conflicting reports, [32, 33] we assessed whether BV2 cells are able to externalize NPs by exocytosis.

The importance of optimizing the pharmaco-kinetics of NP-based medical systems is obviously huge.[8, 34] To avoid accumulation at undesired sites and maximize availability of NPs, one can decrease the captation by the MPS and/or increase the renal clearance. NP captation is a major hurdle to the application of NPs to medicine since the MPS can quickly eliminate intravenously administered NPs from the bloodstream.[9] This can be partially counteracted by an appropriate choice of the NP size and surface chemistry, as mentioned above. Renal clearance prevents NP accumulation in the body thus easing both acute and chronic toxicity.[35] The bio-distribution of NPs intravenously injected in healthy mice was followed by MRI and histological assays.

In the following we will show that innocent magnetic NP scaffolds can be prepared that satisfy the above-mentioned requisites despite the complex behavior of the NP surface charge. We particularly mention the absence of immune-related effects in whole human blood. We also found that NPs as large as 11 nm are effectively cleared by urinary excretion. This finding is unexpected since it is held that inorganic NPs are cleared through the kidneys if their hydrodynamic diameter is $\leq$ 5.5 nm.[19] Many later reports showed renal clearance of NPs smaller than 5.5 nm, [35] and up to now this cutoff has generally been regarded as valid. We discuss this surprising observation in the context of recent results on the function and ultrastructure of the kidneys.

2. Materials and Methods

2.1 Chemicals

Iron pentacarbonyl ($Fe(CO)_5$), oleic acid (OlAc, 90%), oleylamine (OlAm, technical grade, 70%), 1,2-hexadecanediol (97%), 2-[2-(2-methoxyethoxy)ethoxy]acetic acid (MEEA, technical grade), caffeic acid (95%), dopamine hydrochloride, methyl iodide, 1,3-

propanesultone, *N*,*N*-diisopropylethylamine (DIPEA), triethylamine (TEA), trifluoroacetic anhydride (TFAA), 2,2-dimethoxypropane (DMP), LiOH, and Na_2CO_3 were purchased from Sigma Aldrich and used as received. Solvents: methanol (MeOH), ethanol (EtOH, 98%), dibenzyl ether (98%), 1-octadecene (ODE, 90%), acetone (tech. grade), hexane, dimethylformamide (DMF), tetrahydrofuran (THF) and dichloromethane (DCM) were purchased from Sigma Aldrich and used as received. Water for injection (WFI, Ph. Eur.) was purchased at local pharmacies.

2.2 Synthesis of NPs

Synthesis of Iron Oxide (FeOx) NPs

The FeOx NPs were synthesized by modifications of the procedure reported in Ref. [36]. The general procedure is as follows. In a 100-mL three-necked round-bottom flask, equipped with condenser, thermocouple, and rubber septum, OlAc (3.90 g, 13.8 mmol) was dissolved in 30 mL of ODE under stirring and argon atmosphere. The solution was heated to 105 °C and degassed three times by vacuum-argon cycles. After 10 min $Fe(CO)_5$ (600 μL, 4.56 mmol, 0.16 M) was injected through the rubber septum. After 20 min the reaction mixture was heated to 320 °C (heating rate 15 °C/min) and aged at that temperature for 1.5 h. The mixture was then cooled to 120 °C, and air was admitted into the reaction vessel to ensure oxidation of the NPs. After cooling at RT, the reaction crude was precipitated with acetone, and the NPs were collected by centrifugation (3400 *g*, 10 min). The NPs were repeatedly washed with acetone and EtOH and collected by centrifugation (3400 *g*, 10 min). The resulting OlAc-coated NPs were dispersed in hexane at a concentration 1-5 g_{Fe}/L. The iron concentration of the dispersion was measured by the spectrophotometric method described in [23]. The isolated yield was about 50%.

The above procedure with $Fe(CO)_5$:OlAc 1:3 mol/mol gave 11 nm monodisperse NPs. NPs with different size were obtained by varying both the $Fe(CO)_5$:OlAc molar ratio and the reactant concentration as summarized in Table 1.

Table 1. Details of the solvothermal synthesis of OlAc-coated FeOx NPs.

Nominal diameter (nm)	$[Fe(CO)_5]$ (M)	$Fe(CO)_5$: OlAc (mol/mol)	Isolated Yield (%)
3	0.26	1:1	26
11	0.16	1:3	50

17	0.25	1:6	44
22	0.25	1:8	18

Synthesis of Ferrite NPs

Ferrite (MFe_2O_4, M = Mn, Co) NPs were synthesized following the procedure reported in [37] except for the use of 1,2-hexadecanediol instead of 1,2-tetradecanediol. The molar ratio $M(acac)_2$: $Fe(acac)_3$ was 1:2. After the high temperature synthesis, the NPs were repeatedly washed with acetone and EtOH and collected by centrifugation (3400 *g*, 10 min). The resulting OlAc-coated NPs were dispersed in hexane at a concentration 1-5 g_{Fe}/L. The isolated yield was about 30% with respect to Fe.

2.3 Synthesis of Ligands

Synthesis of Dopamine Sulfonate (DS)

Synthesis of dopamine sulfonate (DS) was carried out according to a modification of a previously reported procedure (Scheme 1). See the Supplementary Data for further detail.

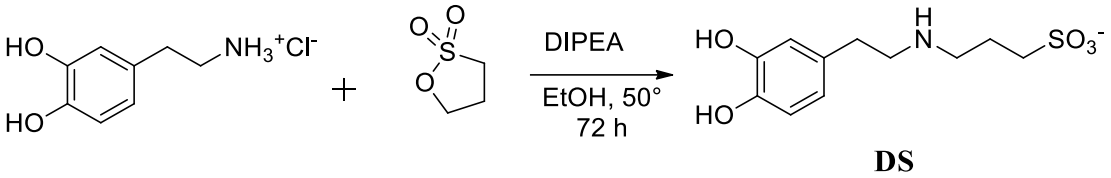

DS

Scheme 1. Synthesis of dopamine sulfonate (DS)

Synthesis of Zwitterionic Dopamine Sulfonate (ZDS)

The published synthesis of zwitterionic dopamine sulfonate (ZDS) involves the double alkylation of the amine group of DS using MeI in basic conditions.[21] This procedure suffers from several drawbacks due to the reactivity of the vicinal aromatic diol. First, dopamine is readily oxidized under basic conditions to dopamine quinone, which easily undergoes self-polymerization. Second, in these conditions MeI can alkylate either or both the phenolic groups. These side reactions make product isolation difficult and lower the yield.

A more effective synthetic procedure was conceived, which involves the protection of the 3,4-dihydroxy moiety as acetonide, followed by the formation of the quaternary ammonium ion and final deprotection. (Scheme 2). In detail, the first step in our synthesis of ZDS is the protection of both the amino group, through the formation of trifluoracetate-dopamine, and the 3,4-dihydroxy moiety by DMP in the presence of a catalytic amount of *p*-toluenesulfonic acid (*p*-TsOH) leading to the formation of the acetonide. Once the 3,4-dihydroxy moiety was protected, the amino protection could be removed at RT under very mild conditions using a solution of LiOH in H_2O/THF. See the Supplementary Data for further detail.

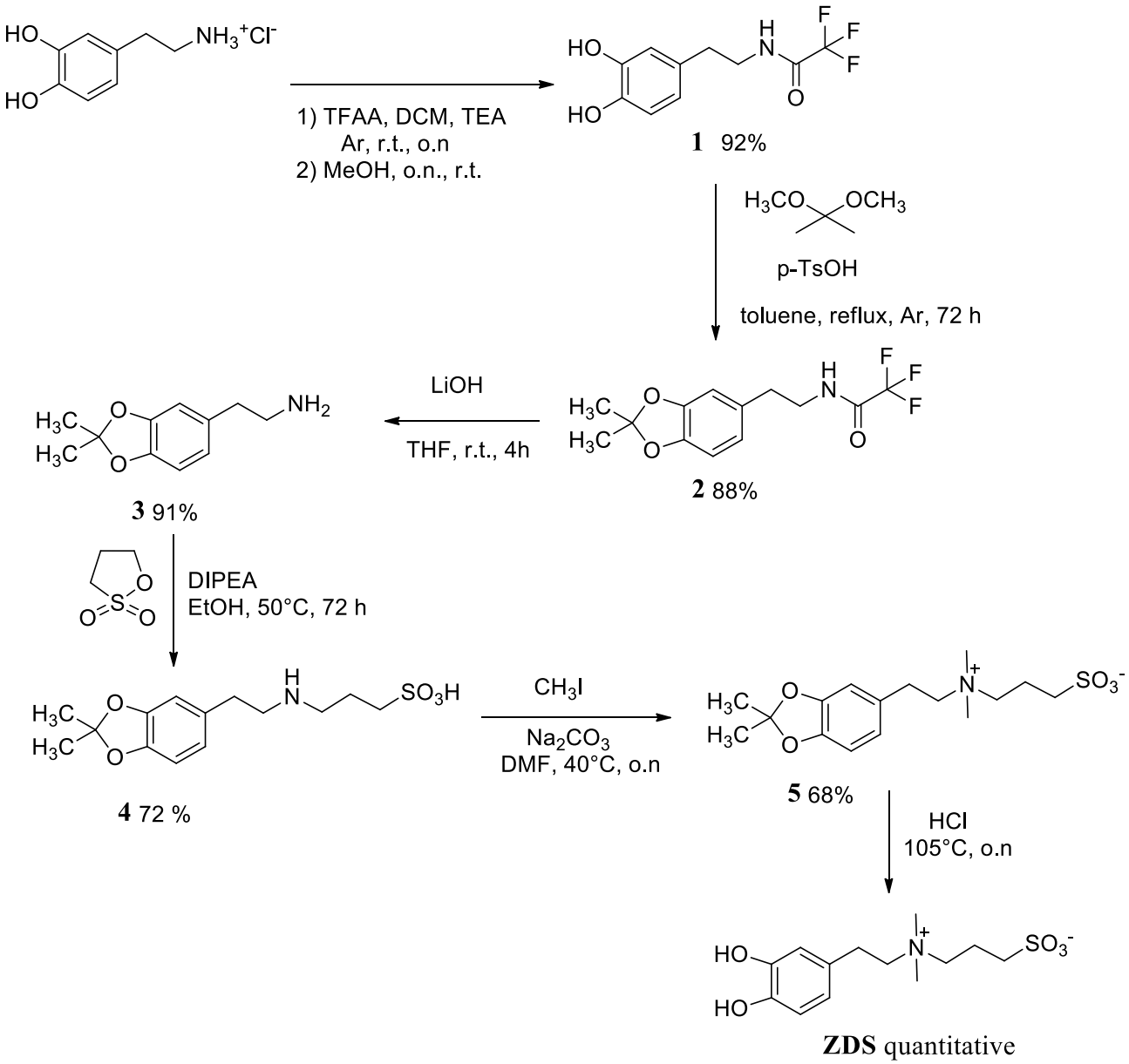

Scheme 2. Synthesis of zwitterionic dopamine sulfonate (ZDS)

Synthesis of coryneine chloride (COR)

Coryneine was prepared starting from compound **3** using acetonide as a protecting group for the vicinal diol. See the Supplementary Data for further detail.

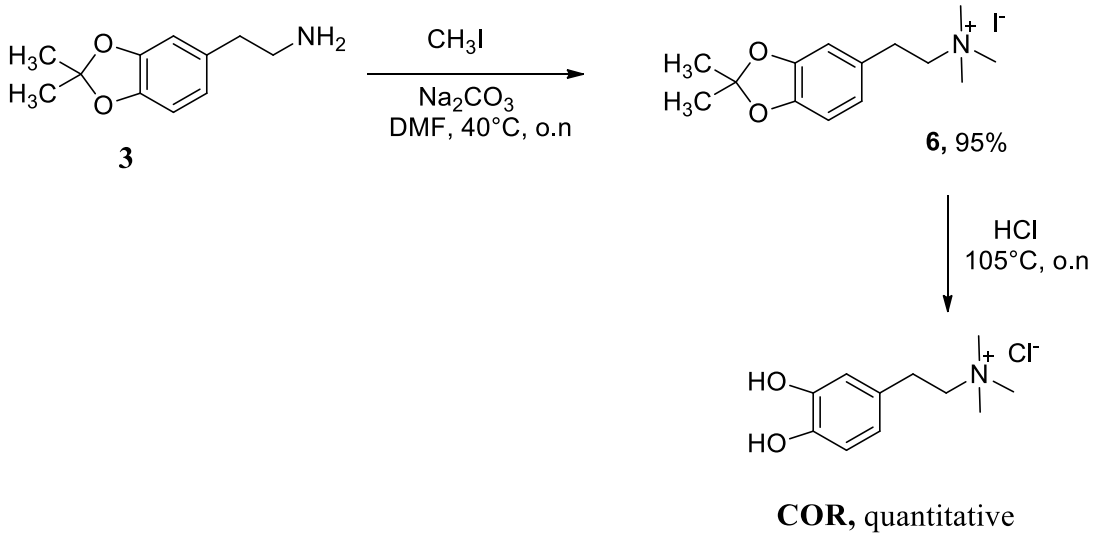

Scheme 3. Synthesis of coryneine chloride (COR)

Ligand Exchange on the NP Surface

Ligand exchange aimed at replacing oleic acid with DS, ZDS, CAF or COR as a NP coating was carried out by a two-step procedure involving MEEA as an intermediate ligand, as previously described for ZDS.[21, 23] The procedure was modified to use a lower ligand : NP ratio. The general procedure is as follows. Dried OlAc-coated NPs (15 mg of Fe) were added to a solution of MEEA (375 μL, 435 mg) in MeOH (1.5 mL). The mixture was stirred for 5 h at 70 °C under nitrogen. The NPs were precipitated by addition of a hexane/acetone 3:1 v/v mixture (16 mL) and collected by centrifugation (3400 *g*, 10 min). The MEEA-coated NPs were added to a solution of ligand (75 mg) in DMF/water 2:1 v/v mixture (18 mL). The mixture was stirred at 70 °C for 12 h under argon. When using CAF, Na_2CO_3 (136 mg) was added to improve the exchange yield. The hydrophilic NPs were precipitated with acetone and redispersed in water. The resulting NPs were purified from the excess ligand by dialysis against water

(MWCO 12500 Da, 24 h). Water for injection (WFI, Ph. Eur.) was used both for ligand exchange and dialysis.

NP samples for immunogenic testing were prepared with care to minimize the content of bacterial endotoxin. Disposable sterile apyrogenic labware was used when commercially available. Otherwise, labware was kept in oven at temperature > 150 °C for 2 days, then washed with aq. NaOH 1 M and rinsed with EtOH before use. WFI was used throughout the procedure.

2.4 Physico-chemical characterization techniques and instruments

^{1}H and ^{13}C nuclear magnetic resonance (NMR) spectra were recorded on a Bruker Avance spectrometer (Bruker, Ettlingen, Germany; ^{1}H: 400 MHz, ^{13}C: 100 MHz).

Transmission electron microscopy (TEM) images, electron diffraction (ED) patterns, electron energy loss spectra (EELS), electron spectroscopy imaging (ESI) maps, and energy dispersive X-ray (EDX) spectra were collected using a Zeiss LIBRA 200FE microscope (Carl Zeiss AG, Oberkochen, Germany) equipped with an Oxford X-Stream 2 EDX spectrometer (Oxford Instruments plc, Abingdon, UK). The TEM specimen was prepared by evaporating in air a drop of diluted NP dispersion on a carbon coated copper grid. The size distribution of the iron oxide cores was obtained analyzing TEM images by the software PEBBLES.[38] PEBBLES is freely available from the authors (http://pebbles.istm.cnr.it).

Chemical composition data were extracted from EELS spectra using Egerton's SigmaL3 software [39] and from EDX spectra using the INCA software (Oxford Instruments, Abingdon, UK).

Ultraviolet-visible (UV-Vis) spectra were recorded on a Thermo Scientific Evolution 600 spectrophotometer.

Fourier-transform infrared (FTIR) spectra were recorded on a Thermo Nicolet NEXUS 670 FTIR spectrometer (Thermo Fisher Scientific, Waltham, MA, USA). The specimen for FTIR was prepared by grinding and pelleting dry NPs with KBr [40] (NP : KBr 1:100 w/w).

Measurement of the NP hydrodynamic diameter and ζ potential was carried by dynamic light scattering (DLS) using a BI 90 Plus (Brookhaven Instruments Corporation, Holtsville, NY, USA). Measurement of hydrodynamic diameter was performed at 25 °C on dialyzed NPs dispersed in WFI or in the complete cell culture medium [Roswell Park Memorial Institute (RPMI)-1640 medium + 5% heat-inactivated fetal bovine serum (FBS)] at a final concentration of *ca.* 50 μg_{Fe}/mL. The volume-weighted NP hydrodynamic diameter was calculated from DLS data using the CONTIN software,[41, 42] which allows for reliable results. The calculation of

NP hydrodynamic diameter by the inversion of DLS correlograms is an exponentially ill-posed problem and its solution critically depends on experimental noise.[43] Therefore, it is of utmost importance that one has full control on all regularization and inversion parameters, which is usually not the case when commercial software is used.

The ζ potential was measured on dialysed NPs dispersed in WFI or phosphate buffered saline (PBS) 1× at a final concentration of *ca.* 50 μg_{Fe}/mL. The pH was adjusted using 10 mM aqueous HNO_3 or tetramethylammonium hydroxide (TMAOH) since it has been shown that NO_3^- and TMA^+ ions do not perturb the stability of uncoated magnetite NPs.[40]

2.5 Methods for uptake and transport of NPs in phagocytic cells

Microglial cultures

BV2 cells. BV2 cells are mouse microglial cells transformed and immortalized by v-raf/v-myc recombinant retrovirus.[44] Cells have morphological, phenotypic and functional characteristics of macrophages and microglia. BV2 cells were provided by Dr F. Aloisi (Istituto Superiore di Sanità, Roma) and grown in RPMI-1640 medium, supplemented with 5% heat-inactivated fetal bovine serum (FBS, endotoxin < 5 EU/mL) (both from Gibco, Life Technologies, Carlsbad, CA).

Primary microglia. Mixed glial cell cultures, containing both astrocytes and microglial cells, were established from postnatal rat Sprague–Dawley pups (P2), as previously described. [45] Briefly, after dissection, hippocampi and cortices were dissociated by treatment with trypsin and DNase-I for 15 min at 37 °C, followed by fragmentation with a fire-polished Pasteur pipette. Dissociated cells were plated on poly-L-lysine-coated T75 flasks in minimal essential medium (E-MEM, Invitrogen) supplemented with 20% FBS and glucose (5.5 g/L). Microglial cells were harvested from 7-10 days-old cultures by orbital shaking for 30 min at 1300 rpm and plated on poly- L-ornithine-coated tissue culture dishes or glass coverslips. In a set of experiments cells were stained with the PKH67 green fluorescent membrane dye (2 μM, Sigma-Aldrich, Inc.) and added to purified microglial cultures previously exposed to NPs. All experimental procedures followed the guidelines established by the European Directive 2010/63/EU and Italian Legislation (L.D. no. 26/2014). All efforts were made to minimize the number of animals used and their suffering.

Quantification of NP internalization by microglial cells

Cells were seeded on 10 cm-plates, (0.5-1.0 · 10^5 cells/cm^2), grown for 24 h and exposed to NPs dispersed in culture medium to different final concentrations and for different times. The cells were then washed five times with PBS to remove all non-internalized NPs, detached from plates and collected by centrifugation at 800 *g* for 5 min. Pellets were resuspended in distilled water, and protein content measured by the BIO-RAD-DC protein assay (Bio-Rad Laboratories, Inc., Hercules, California, USA). The cell pellets were digested and treated with excess disodium 4,5-dihydroxy-1,3-benzenedisulfonate (tiron) at pH ≅ 7 for 1 h to form the red complex $[Fe(tiron)_3]^{9-}$ that was spectrophotometrically quantified as previously described [23] (see the Supplementary Data for the detailed procedure). Cellular iron concentration *C*(Fe) is expressed as the mass ratio between cellular iron and protein ($\mu g_{Fe}/mg_p$). When MFe_2O_4 (M = Mn, Co) NPs were used, the *C*(Fe) was scaled in accordance with the chemical composition of the NP core before comparing it with the *C*(Fe) of FeOx NPs.

Statistical analysis of NP internalization data

Results from replicate cultures of one representative experiment or from replicate experiments are presented as mean ± SEM, standard deviation and range. Statistical analysis was carried out by JASP 0.9.2 and the R package PMCMR. Since most datasets do not satisfy the equal-variance requirement, as tested by Levene's test, the difference between mean values of different treatments was tested by the ANOVA method corrected for heteroscedasticity using the Brown-Forsythe and Welch corrections, and by the non-parametric Kruskal-Wallis test. Multiple comparisons between treatment means were carried out by the Conover test [46] adjusted by the Benjamini-Hochberg false discovery rate (FDR) method.[47]

Prussian Blue staining and imaging

NP-treated cells were extensively washed with PBS and fixed for 30 min in 4% paraformaldehyde (PFA), incubated for 30 min with freshly prepared Perls' reagent (4% potassium ferrocyanide/12% HCl, 1:1 v/v), washed in PBS and mounted onto microscope slides. Bright-field and fluorescent images were acquired at 40× magnification using a Leica DMI 4000B microscope (Leica Microsystem GmbH, Wetzlar, Germany), equipped with differential interference contrast (DIC) microscopy.

For histological analysis of liver, kidney, spleen and dorsal muscle, mice were sacrificed after the last magnetic resonance imaging (MRI) session, and perfused with 0.01 M PBS for 5 min and then with PBS-buffered 4% formaldehyde for 15 min. The organs were

collected, dehydrated and embedded in paraffin. Tissues were cut with a slice thickness of 8 μm and the sections were stained with Perls' reagent following the same protocol used for cells. Finally, the slices were counterstained with nuclear fast red (NFR) for 5 min. Three sections from each tissue were photographed at 20× magnification under a Zeiss Axioskop microscope equipped with an EOS 40D Canon Camera (Ōta, Tokyo, Japan).

Cell viability assay

Microglia viability was analysed by fluorescence staining with propidium iodide (PI, 1 mg/mL; Molecular Probes, Life Technologies Ltd., Paisley, UK) for dead cells, with calcein-AM (0.5 mg/mL, Invitrogen, Life Technologies Ltd.) for viable cells and with Hoechst 33342 as a DNA/nuclear marker (8.1 mM; Molecular Probes, Life Technologies Ltd.). Incubation was performed for 20 min in E-MEM (Invitrogen) supplemented with 20% FBS (Gibco) and glucose (5.5 g/L) at 37 °C and 5% CO_2. Fluorescence images were acquired by Leica DMI 4000B microscope. The percentage of cell death was calculated as the ratio of PI^+/$calcein^-$ cells (dead) to the total number of Hoechst-stained microglia in 15 fields/condition.

In vitro MRI

The measurement of the relaxation rate of NPs and the establishment of the minimal concentration of Fe detectable by MRI were carried out in a phantom study. The phantoms were prepared in tubes containing H_2O or mouse urine to create a localizable dispersion containing different concentrations of NPs in spots. For the 3 nm/FeOx/ZDS NPs the final concentration of Fe in the phantoms was 1.5, 3, 6, 12, 24, 48, 96, 128 and 160 μg/mL, respectively. On the other hand, for the 11 nm/FeOx/ZDS NPs the final concentration of Fe in the phantoms was 1.5, 3, 6, 12, 24, 48, 96, and 128 μg/mL.

To establish the minimal number of NP-labeled BV2 cells that produced significant decrease in T_2 values or signal intensity (SI), $3 \cdot 10^5$ BV2 cells were seeded in a 30 mm-plates for 1 day. After 6 h of incubation with 100 μg/mL of 11 nm/FeOx/ZDS NPs, BV2 cells were washed three times with 0.01 M PBS to remove excess of NPs and then suspended in 0.01 M PBS. Control BV2 cells were incubated in absence of NPs. Different numbers of control and NP-labeled BV2 cells were embedded in 900 μL of 2% low-melting agarose gel (Sigma-Aldrich) into tubes with 5 mm diameter. NP phantoms were constructed *via* dilution of BV2 cells to concentrations of 0, $111 \cdot 10^3$, $166 \cdot 10^3$, $333 \cdot 10^3$, $666 \cdot 10^3$, and $1000 \cdot 10^3$ cells/mL. Sample tubes containing NPs were placed around a homogeneous 20 nM $CuSO_4$ solution. Further, all the tubes were placed at the center of the magnet bore.

All the *in vitro* imaging was performed into a vertical 4.7 T Bruker Avance II 200 system with 15 cm bore (Bruker, Ettlingen, Germany). For BV2 cells, imaging of phantoms was performed using T_2 MAP and T_2-weighted sequences, whereas for the 11 nm/FeOx/ZDS NPs, a T_1 MAP analysis was also performed. In detail, the sequences are as follows.

T_2-weighted images were acquired using the fast low angle shot (FLASH) sequence. The imaging parameters were as the follows: echo time (TE) = 5 s; repetition time (TR) = 200 ms; number of averages = 2; number of repetition = 1; flip angle = 40°; field of view (FOV) = 4.0 cm x3.0 cm; slice thickness = 3 mm; number of slice = 1; in-plane resolution = 312×312 $\mu m^2/pixel^2$.

T_2 maps were acquired using the multi-slice multi-echo (MSME) sequence. The imaging parameters were as the follows: TE = 10; Effective ET = 10-80 ms with a total of 8 echoes and echo length of 10 ms; number of averages = 4; number of repetition = 1; FOV = 4.0 cm x 3.0 cm; slice thickness = 3 mm; number of slice = 1; in-plane resolution = 312×312 $\mu m^2/pixel^2$.

T_1 maps were acquired using the Rapid Acquisition with Refocused Echoes - variable repetition time (RARE-VTR) sequence. The imaging parameters were as the follows: TE = 10 s; Rare factor = 1; TR = 6000 ms, 3000 ms, 1500 ms, 800 ms, 400 ms, 200 ms, 100 ms and 50 ms; number of averages = 1; number of repetition = 8; FOV = 4.0 cm x3.0 cm; slice thickness = 3 mm; number of slice = 1; in-plane resolution = 312×312 $\mu m^2/pixel^2$.

T_1 and T_2 values, as well as T_2-weighted signal intensity induced by NPs at each concentration were determined within regions of interest (ROIs) of about 4 mm^2.

2.6 Methods for immune/inflammation-related effects.

Limulus amebocyte lysate (LAL) assay

Contamination of endotoxin (bacterial lipopolysaccharide, LPS) in NPs was performed with the chromogenic Pyrochrome LAL assay (Associates of Cape Cod Inc., East Falmouth, MA, USA), modified and adapted for the use on nanoparticulate samples.[48] At least three concentrations of each particle were tested, which were further checked for interference with the optical readout and an acceptable recovery rate (100 ± 20%). Endotoxin contamination of NPs was expressed as endotoxin units (EU) per mg of Fe.

Whole blood assay (WBA)

Whole blood was collected in ethylenediaminetetraacetic acid (EDTA) buffer from healthy donors, after informed consent. NPs were pre-incubated in fresh autologous plasma for 1 h at

37°C prior to addition to WBA tubes. WBA tubes were prepared with 750 of RPMI-1640 medium (GIBCO by Life Technologies, Paisley, UK) alone or containing LPS (2.5 ng/mL), the selected NPs, or both, on which 250 µl of anti-coagulated whole blood were added. By considering the concentration of the stock NP suspensions and real-life situations, final NP concentrations selected for use in the WBA were never above 10 µg/mL. The experimental concentration of each NP type was chosen from preliminary dose-response experiments and by taking in consideration the measured level of endotoxin contamination. NP concentrations were: ZDS-coated FeOx NPs, 2 µg/mL; DS- and CAF-coated FeOx NPs, 1 µg/mL; ZDS-coated $CoFe_2O_4$ NPs, 8 µg/mL; and ZDS-coated $MnFe_2O_4$ NPs, 7 µg/mL. Blood tubes were incubated 24 h at 37 °C, after which 100 µL of 5% Triton-X (Sigma-Aldrich, Inc.) was added, to lyse cells. Tubes were inverted 5 times until lysis was complete. Lysed blood was frozen at -80°C until assayed.[49]

Kinetic model of inflammation

To assess the interference of NPs with a normal innate/inflammatory response, an *in vitro* kinetic model of inflammation was used, based on primary monocytes isolated from the blood of healthy donors. Briefly, peripheral blood mononuclear cells (PBMCs) were isolated by gradient density centrifugation on Ficoll-Paque PLUS (GE Healthcare, Bio-Sciences AB, Uppsala, Sweden). Monocytes were isolated from PBMCs using CD14 magnetic separation (Monocyte Isolation II kit; Miltenyi Biotec, Bergish-Gladback, Germany). Purity of monocytes was determined by differential counting on cytosmears stained with Diff-Quik (Medion Diagnostics, Duedingen, Switzerland). Viability was assessed by Trypan Blue dye exclusion. Monocyte purity and viability was always >95%.

Monocytes (2.5×10^6 per well) were cultured in 12-well plates (Corning Costar, Milano, Italy) in RPMI-1640 medium (GIBCO), supplemented with 50 µg/mL gentamicin (Sigma-Aldrich, Inc.) and 5% heat-inactivated human AB serum (Sigma-Aldrich, Inc.). Temperature and stimuli were controlled to mimic the microenvironment found in inflamed tissue. CCL2 (20 ng/mL), LPS (5 ng/mL), TNFα (10 ng/mL), and IFNγ (25 ng/mL) were added and removed sequentially (cytokines purchased from R&D Systems, Minneapolis MN, USA) as follows. From 0 to 2 h, monocytes were exposed to CCL2. At 2 h, cells were washed, and exposed to a cocktail of LPS, TNFα, and the 11 nm ZDS-coated FeOx NPs (2 µg/mL, pre-incubated 1 h at 37 °C in heat-inactivated human AB serum) or solvent, and the temperature increased from 37 °C to 39 °C. At 7 h, IFNγ (25 ng/mL) was added. After 15 h, medium was

refreshed with or without NPs, and temperature was restored to 37 °C. Supernatants were collected, and cells were harvested in 700 µl Qiazol (Qiagen, Hilden, Germany) for RNA extraction. Supernatant and cell collection occurred at 0, 4, 8, 15, and 24 h, and all samples stored placed at -80 °C until testing.

Cytokine measurements

Measurements of IL-1β and IL-1Ra were conducted with enzyme-linked immunosorbent assay (ELISA) kits (R&D Systems). Samples were assayed in duplicate, and absorbance was measured at 450 nm and corrected for background at 550 nm. Cytokine levels measured in culture supernatants are expressed as pg/10^6 plated monocytes, whereas cytokines measured in the WBA are expressed as pg/mL blood.

RNA extraction and real time PCR

RNA purification from cell samples collected in Qiazol (see above) was performed using the miRNeasy kit (Qiagen), and quantified with a ND-1000 spectrophotometer (NanoDrop Technologies, Wilmington, DE, USA). cDNAs were reverse-transcribed from total RNA (100 ng) according to the QuantiTect Reverse Transcription Kit (Qiagen) instructions. Three separate reverse transcriptions were performed for each sample, and an identical reaction without the reverse transcriptase was run, as negative control. Polymerase chain reaction (PCR) was performed by a Rotor-Gene™ 3000 (Corbett Research, Doncaster, Victoria, Australia), using the QuantiTect SYBR Green PCR master Mix (Qiagen). The final reaction contained 12.5 µL 2x QuantiTect SYBR Green PCR Master Mix, 0.3 µM of each primer and 2.5 µL of cDNA in a total volume of 25 µL. PCR conditions were 95 °C for 15 min, followed by 40 cycles of 95 °C for 15 s, 50-60 °C for 30 s and 72 °C for 30 s. Primer sequences were supplied by Qiagen both for target (*IL1B* and *IL1RN*) and housekeeping (*GAPDH*) genes. Relative gene expression was calculated using the efficiency correction method.[50]

Statistical analysis of cytokine expression and production data

Data of cytokine expression and production are presented as mean ± standard deviation (SD) of values from replicate cultures of one representative experiment or of replicate donors. Statistical significance was calculated by Student's *t*-test. A p value < 0.05 was considered as suggesting a statistically significant difference.

2.7 Methods for biodistribution of ZDS/FeOx NPs in mice

Animals and experimental protocols

The procedures concerning animal care, procedures and euthanasia were carried out in accordance with Italian laws and with the current European Union Council (2010/63/UE) guidelines for the use of laboratory animals in chronic studies. The *in vivo* MRI experiments were approved and authorized by the National Ministry of Health - University of Milan Committee (Approval number 12/12-30012012). The study was conducted applying the ARRIVE guidelines.

To study NP biokinetics, CD1 male mice (30-35 g body weight; Charles River, Calco, Italy) were injected with: (*i*) physiological solution (n = 3), (*ii*) 1 or 4 mg Fe/kg of 3 nm/FeOx/ZDS NPs (n = 5 and 1, respectively), (*iii*) 1 or 4 mg Fe/kg of 11 nm/FeOx/ZDS NPs (n = 5 and 1, respectively). NPs were administered by tail vein injection over 5 seconds. The injected NP volume was ~150 μL, with individual injection volumes adjusted on animal weight.

In vivo mouse MRI

Mice were scanned with a Bruker 4.7 T vertical-bore imaging system (AMX3 Bruker, Ettlingen, Germany). The mice were anesthetized with 2% isofluorane (Merial, Lyon, France) in 100% O_2 in an induction chamber, then fixed on a MR-compatible stereotactic holder and placed into a 3.8 cm diameter birdcage coil. The anesthesia was maintained with 1% isofluorane in 100% O_2, and respiration rate was continuously monitored during MRI measurements using a MR-compatible Small Rodent Air Heater System (SA Instruments, Inc., New York, USA), also used to synchronize image acquisition with the respiration. Breathing and body temperature were maintained around 30 breaths-per-minute and at 37 °C, respectively. For all the animals, MRI scanning started with baseline scans prior to the injection of the NPs.

For mice treated with 11 nm/FeOx/ZDS NPs, T_2-weighted MR images were collected at 5, 10, 15, 30 and 60 min post-injection without removing the mouse from the coil. T_2-weighted and T_2 MAP images were also collected at 2 and 4 h and 1, 2, 7 and 14 days from injections. For mice treated with 3 nm/FeOx/ZDS NPs, T_2-weighted MR images were collected at 5, 10, 15, 30 and 60 min post injection without removing the mouse from the coil, and then at 3 and 6 h.

MAP and T_2-weighted abdominal imaging needed respiratory gating and used the same MSME and FLASH sequence used in *in vitro* MRI experiments. In detail, for T_2 MAP scans, 10 slices with 1.3 mm thickness were positioned in the axial plane with 1.0 mm interslice gap,

whereas for T_2-weighted scans, 8 slices with 1.0 mm thickness were positioned in the coronal plane with 0.5 mm interslice gap.

Analysis of MRI data was performed using custom software implemented in the Python environment. Processing stages for quantification of T_2 and of T_2 SI data included (*i*) manual track of the ROIs, (*ii*) translation of the ROI over all images in the time-course images, and (*iii*) automated T_2 value calculation or T_2 SI within the ROI. Analysis of T_2 SI involved normalization of intensity within each image by signal amplitude of the adjacent $CuSO_4$ phantom to correct for temporal fluctuations in hardware sensitivity and scan-to-scan differences in the pulse power/receiver gain settings.

Statistical analysis of MRI data

The data are expressed as mean value ± SD. Statistical analysis of T_2 MAP data was performed by one-way ANOVA followed by Dunnett's Multiple Comparison Test. The T_2* SI data were instead analyzed by Kruskal–Wallis followed by Dunnett's Multiple Comparison Test.

3. Results and Discussion

We compared the biological effects of NPs belonging the class of spherical spinel ferrite NPs coated by short-chain catechol-based (zwitter)ionic ligands with diameter from 3 to 22 nm. We We varied core composition, size, and coating of the NPs (Figure 1). The latter two properties are reported to strongly affect the interaction of NPs with biological systems.[27] We considered three ferrites MFe_2O_4 (M = Mn, Fe, Co), four coating ligands [dopamine sulfonate (DS), zwitterionic dopamine sulfonate (ZDS), caffeic acid (CAF), and coryneine chloride (COR)] and four diameters (3, 11, 17, and 22 nm). Clearly, a full factorial experimental design would require a very large number of NP types (3×4×4 = 48). We then fell back to a one-factor-at-a-time design entailing the choice of pivotal reference NPs, which are varied by a single parameter at a time. This design requires of 1+2+3+3 = 9 NP types. The controlled variation of individual physico-chemical parameters across different NP batches adheres to the recent tenets about the investigation of the biological effects of NPs.[3, 51]

As reference NPs, we selected 11 nm iron oxide NPs coated with ZDS. [21-23, 52] These NPs are colloidally very stable, do not significantly adsorb proteins, and are scarcely internalized by HeLa and HepG2 cells. The NPs with varied parameters are: (*i*) ZDS-coated iron oxide NPs with diameter 3, 17, and 22 nm, (*ii*) ZDS-coated mixed ferrite (MFe_2O_4, M = Mn, Co) NPs, and (*iii*) 11 nm iron oxide NPs coated with DS, CAF, and COR. CAF-coated

ferrite NPs [53, 54] were previously shown to passively accumulate in a mouse model of glioblastoma.[55] COR-coated NPs have not yet been reported to the best of our knowledge. The selected ligands are low molecular weight (MW) molecules (182–304 dalton). All have a catecholic (3,4-dihydroxyphenyl) moiety, able to strongly bind to the inorganic core,[56, 57] and a short (zwitter)ionic [14, 23] tail endowing stability in aqueous media (Figure 1).

3.1 Synthesis and morphology of NPs

Iron oxide (FeOx) NPs were synthesized by a thermal decomposition process which yielded monodisperse spherical NPs.[36] Electron diffraction (ED) showed that these NPs have the cubic ferrite crystal structure (Figure S1, Supplementary Data). TEM images of selected NPs are shown in Figure 2. (see Figure S2, Supplementary Data for other TEM images) The NP (core) size measured using the PEBBLES software is reported in Table 2 (see Figure S3, Supplementary Data for NP size histograms). The as-synthesized NPs are coated with oleic acid (OlAc) in the form of oleate as demonstrated by comparing the FTIR spectra of the NPs, Fe(III) oleate, and OlAc. (Figure S4, Supplementary Data).

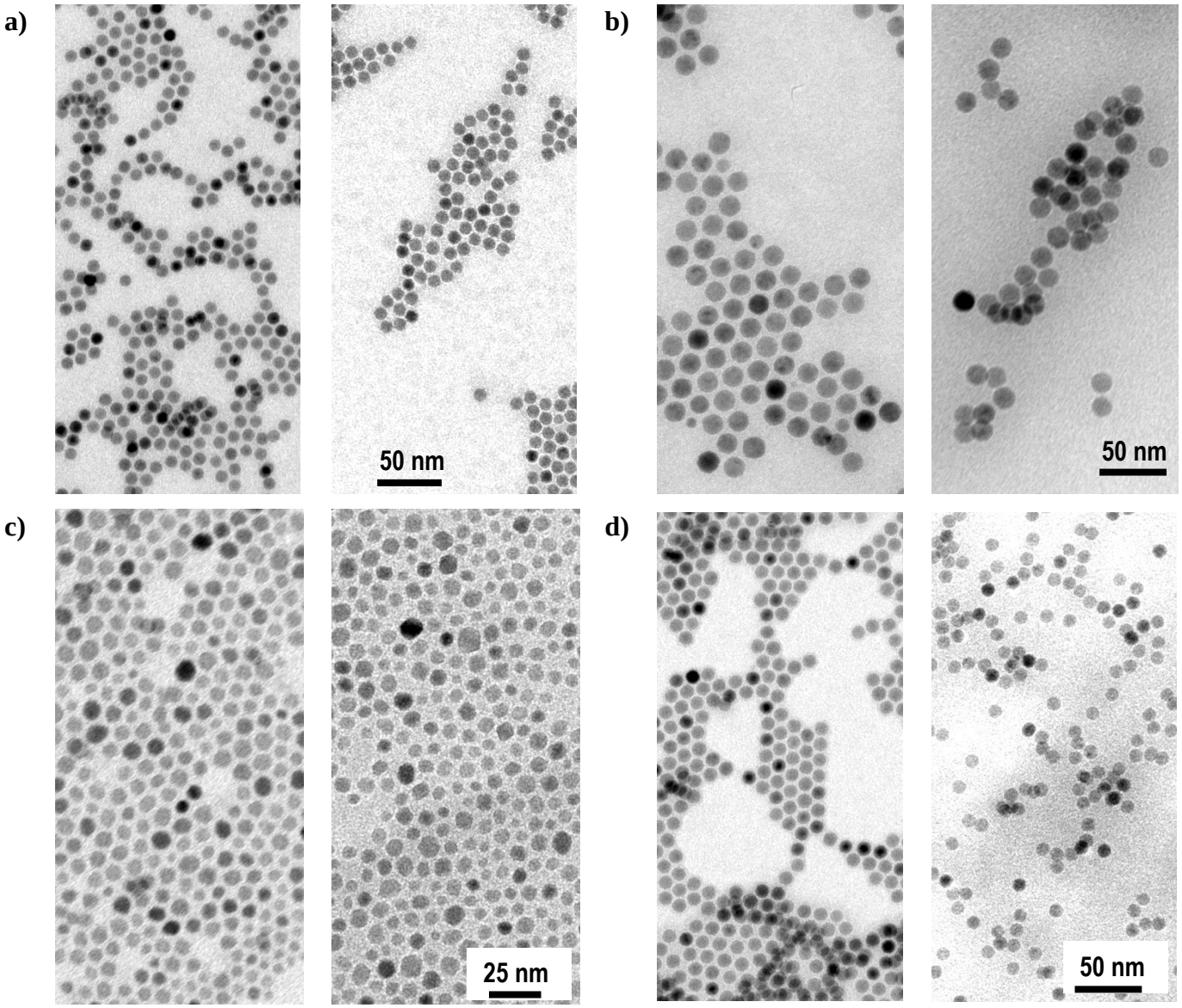

Figure 2. TEM images of NPs before (left) and after (right) ligand exchange. a) Reference 11 nm/FeOx/ZDS NPs; b) 17 nm/FeOx/ZDS; c) 7 nm/$MnFe_2O_4$/ZDS; d) 11 nm/FeOx/CAF.

Table 2. Size of NPs before and after ligand exchange measured from TEM images. The number of measured NPs *N* is reported along with the median $\langle d \rangle$, standard deviation σ_d, and dispersion index $\sigma_d/\langle d \rangle$ of the diameter distribution. The property that distinguishes a NP type from the reference NPs (11 nm FeOx with ZDS coating, first row) is highlighted in bold.

			As synthesized				After ligand exchange			
Nominal size	Core	Final coating	*N*	$\langle d \rangle$ (nm)	σ_d (nm)	$\sigma_d/\langle d \rangle$	*N*	$\langle d \rangle$ (nm)	σ_d (nm)	$\sigma_d/\langle d \rangle$
11	**FeOx**	**ZDS**	1547	10.3	0.4	4%	1003	10.7	0.6	5%
3	FeOx	ZDS	2873	3.3	0.5	14%	204	3.2	0.4	14%
17	FeOx	ZDS	1293	16.7	0.8	5%	306	16.8	0.8	5%
22	FeOx	ZDS	2014	22.6	1.6	7%	265	21.8	1.6	7%
7.5	**$CoFe_2O_4$**	ZDS	1762	7.4	1.3	18%	233	7.1	1.4	20%
7.5	**$MnFe_2O_4$**	ZDS	2006	7.8	1.5	20%	1670	7.4	1.3	18%
11	FeOx	**DS**[a]	1018	10.7	0.6	6%	2389	10.9	0.8	7%
11	FeOx	**CAF**[a]	1018	10.7	0.6	6%	2298	10.8	0.8	7%
11	FeOx	**COR**[a,b]	1018	10.7	0.6	6%	69	10.8	0.5	5%

[a] These sample were prepared starting from a single batch of FeOx/OlAc NPs.

[b] The size of the ligand-exchanged NPs refers to primary NPs within aggregates.

Manganese and cobalt ferrite NPs were synthesized following a different thermal decomposition procedure.[37] Despite some effort, we were not able to synthesize monodisperse spherical 11-nm mixed ferrite NPs since shape and dispersion were strongly dependent on the NP size. The best compromise we could find was to use spheroidal 7.5 nm NPs with dispersion ≅ 20% (see Figure 2 and Table 2). They have cubic ferrite crystal structure (Figure S1, Supplementary Data). EELS and EDX data show that both ferrite NPs are slightly deficient in the divalent metal M = Mn, Co (Table **Error! Reference source not found.**, Figures S5-S6, Supplementary Data). Elemental maps obtained by ESI show that Fe and the divalent metal are both present in all NPs. (Figure S7, Supplementary Data)

Table Error! Reference source not found.. Composition of MFe_2O_4 NPs by EELS and EDX spectroscopy.

	Fe : M atomic ratio	
M	EELS	EDX
Co	3.0 ± 0.3	3.1 ± 0.1

Mn	2.9 ± 0.2	2.8 ± 0.2

To replace the pristine oleic acid coating of the NPs with the ligands in Figure 1, we used a two-step ligand exchange.[21] First, oleic acid is replaced with polyether acid MEEA to make the NPs more hydrophilic. After isolation, the NP can be dispersed in a DMF solution of the target ligand. The second ligand exchange is driven by the stronger iron-binding ability of the catechol moiety with respect to that of the carboxylic acid group. The procedure was monitored by FTIR spectroscopy (Figure S4, Supplementary Data). The pristine OlAc coating was successfully replaced with the four hydrophilic ligands. Aqueous dispersions of ZDS-, DS-, and CAF-coated NPs ($C \approx 1$ mg_{Fe}/mL) did not show any sign of precipitation or turbidity after more than 1 year. COR-coated NPs gave turbid suspensions that precipitated in a few hours. The NP crystal phase (Figure S1, Supplementary Data), shape and size (Figure 2, Table 2, and Figure S2, Supplementary Data) are unaffected by the ligand exchange procedure. The NP median diameter changes by tenths of nanometer and the dispersion index varies by less than 2%. TEM images of COR-coated NPs show thick, large NP aggregates. A detailed TEM investigation (Figure S2j, Supplementary Data) showed that the aggregation did not involve an agglomeration of the inorganic cores.

3.2 Colloidal behavior of the NPs in aqueous media

The colloidal behavior of ligand-exchanged NPs in aqueous dispersion was investigated using different techniques based on DLS. The volume-weighted mean hydrodynamic diameter D of the NPs was calculated analyzing the DLS correlograms by the CONTIN software.[41, 42] and is reported in Table 3.

For ZDS-, DS-, and CAF-coated NPs dispersed in WFI, the volume-weighted distribution of the hydrodynamic diameter comprises a single peak and D is close to the median TEM core diameter $\langle d \rangle$. Therefore, the NPs are well dispersed in water and no significant amount of NP aggregates is present.

The D values of NPs just after dispersion in the cell culture medium (RPMI added with 5% FBS) and after 6 h are not significantly different and both are close to the values in WFI. (Table 3). No appreciable protein adsorption or aggregation occurred, perhaps except the case of CAF-coated NPs. Detecting NP size changes by DLS could be hampered by the presence of proteins To improve sensitivity to size, we monitored the intensity of the scattered light (I_s) over time (Figure S8, Supplementary Data). The analysis of I_s during a 6 h interval after

dispersion in the BV2 cell culture medium showed that ZDS-coated NPs and, to a slightly lesser degree, DS- and CAF-coated NPs are colloidally stable in the cell culture medium and can interact with cells in culture as well-dispersed protein-free NPs, whereas COR-coated NPs are present as large aggregates. Serum protein adsorption onto ZDS- and DS-coated FeOx NPs (d = 8.0 nm, $D \approx$ 10 nm) was previously investigated by size exclusion chromatography (SEC).[21] The SEC results indicated no protein adsorption on NPs coated with ZDS but significant adsorption on DS-coated NPs in 10% FBS, in contrast to our results. It was later shown that ZDS-coated FeOx NPs (d = 5.3 nm, $D \approx$ 9.5 nm) have minimal non-specific affinity toward serum proteins also *in vivo* in mice.[22]

Table 3. Volume-weighted mean hydrodynamic diameter D of NPs dispersed in WFI and in the BV2 cell culture medium. The property that distinguishes a NP type from the reference NPs (11 nm/FeOx/ZDS, first row) is highlighted in bold.

			D (nm) (mean ± SD, n = 10)		
Nominal size	Core	Final coating	WFI	Culture medium – 0 h	Culture medium – 6 h
11	**FeOx**	**ZDS**	12 ± 0.5	13 ± 1	13 ± 2
3	FeOx	ZDS	5.8 ± 0.5	9 ± 1	9 ± 1
17	FeOx	ZDS	20 ± 1	16 ± 3	18 ± 2
22	FeOx	ZDS	21 ± 3	25 ± 4	17 ± 5
7.5	**$CoFe_2O_4$**	ZDS	12 ± 1		
7.5	**$MnFe_2O_4$**	ZDS	10 ± 1		
11	FeOx	**DS**	19 ± 1	20 ± 3	17 ± 3
11	FeOx	**CAF**	18 ± 1	20 ± 7	44 ± 7
11	FeOx	**COR**	260 ± 40	210 ± 40	210 ± 40
	Cell culture medium			10 ± 1	

To better understand the surface chemistry and colloidal stability of the NPs, we measured the ζ potential of the NPs dispersed in PBS 1× (pH = 7.4) as reported in Table 4. The ζ potential of COR-coated NPs could not be measured because of aggregation. While DS- and

CAF-coated NPs have slightly negative ζ potential, ZDS-coated NPs display strongly negative values (–11 to –28 mV) despite the ZDS molecules are neutral. Clearly, this behavior cannot be explained based on the ligand charge. Zwitterionic sulfobetaine micelles preferentially adsorb anions and display negative ζ potential.[58] Since the outer surface of ZDS-coated NPs is structurally similar to that of zwitterionic micelles, anion adsorption can account for the observed negative values. To support this hypothesis, we investigated how the ζ potential of ZDS-, DS-, and CAF-coated 11 nm FeOx NPs varies with pH, using dispersions of NPs in WFI.

Table 4. ζ potential of NPs dispersed in PBS 1×. The property that distinguishes a NP type from the reference NPs (11 nm/FeOx/ZDS, first row) is highlighted in bold.

Nominal size	Core	Final coating	ζ (mV) (mean ± SD, n = 10)
11	**FeOx**	**ZDS**	–16 ± 2
3	FeOx	ZDS	–28 ± 2
17	FeOx	ZDS	–18 ± 2
22	FeOx	ZDS	–29 ±3
7.5	**$CoFe_2O_4$**	ZDS	–22 ± 3
7.5	**$MnFe_2O_4$**	ZDS	–14 ± 3
11	FeOx	**DS**	–2 ± 4
11	FeOx	**CAF**	–8 ± 6

The dispersions of ZDS- and DS-coated NPs in WFI have pH close to 7 while that of CAF-coated NPs is slightly basic (pH 7.7) probably because of partial hydrolysis of the caffeate anion.[59] The ζ potential of these dispersions is very close to 0 mV in all cases. It is noteworthy that dispersions of these NPs in WFI at concentration ≈1 g_{Fe}/L are stable for a few years. The pH was adjusted by adding aqueous HNO_3 or TMAOH. The behavior displayed by the NPs is somewhat complex but it is reproducible across measurements and for different NP batches (Figures 3 and S9,Supplementary Data).

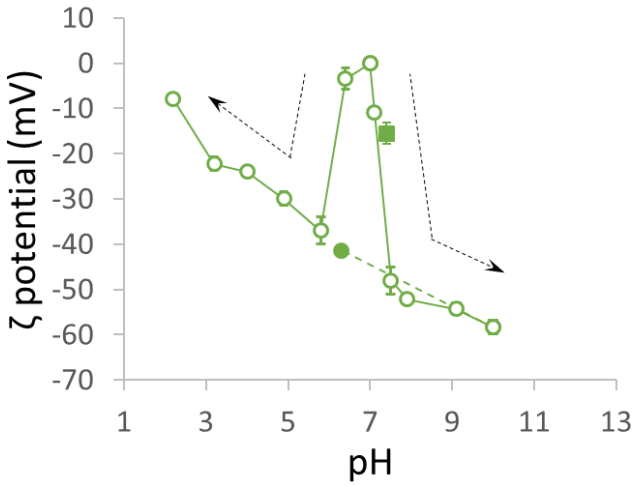

Figure 3. ζ potential of 11 nm ZDS-coated FeOx NPs at different pH. The ζ potential was measured starting from NPs in WFI (pH = 7) and then adjusting the pH by adding aqueous HNO_3 or TMAOH (hollow circles). The dashed arrows indicate how the pH was varied. The datum measured after decreasing the pH from the highest value is shown as a solid circle. The ζ potential in PBS 1× is shown as a solid square. Error bars correspond to the standard error of the mean; they are smaller than the symbol in many data points. The green lines are just a guide to the eye.

Starting from pH = 7, the ζ potential of 11 nm ZDS-coated FeOx NPs quickly becomes negative after addition of both acid and base. Since the quaternary ammonium and sulfonate groups of ZDS (Figure 1) are charged in the investigated pH range, the observed behavior can be ascribed to the preferential adsorption of OH^- (pH > 7) or NO_3^- (pH < 7) anions. Addition of base makes the ζ potential more negative because more OH^- anions are adsorbed. The addition of acid shifts the ζ potential toward 0 mV since at low pH the negatively charged NPs attract the abundant H_3O^+ cations thereby reducing the ζ potential. When the dispersion is brought from pH 12 to pH 6.3 by adding HNO_3, the ζ potential remains negative because the neutralized OH^- ions are replaced by NO_3^- anions. Thus, the "slanted Mexican hat" shape of the ζ – pH curve of ZDS-coated NPs can be easily understood on the basis of preferential ion adsorption. [58]

A more detailed discussion can be found in the Supplementary Data where it is also shown that the aqueous dispersions of DS-coated and CAF-coated NPs display a similar behavior. Our results agree with the negative ζ potential of other zwitterionic NPs.[15] The complex ζ – pH behavior of these NPs depends more on the preferential anion adsorption at the

organic coating than on the charge distribution of the coating ligands. The predominant role of the preferential ion adsorption unfortunately made quite similar the ζ potential of NPs coated with ligands having nominally different molecular charge. The electrolytic composition of the dispersion medium is a key factor in the NP surface charge, which has to be taken into consideration when designing NPs for biological applications.

3.3 Relaxometry of NPs

The T_1 and T_2 relaxation times of 3 and 11 nm/FeOx/ZDS NPs samples with different concentrations of Fe were calculated using a custom software. The longitudinal (R_1) and transverse (R_2) relaxation rates linearly depend on iron concentration (Figures S10 and S11, Supplementary Data). The relaxivities r_1 and r_2 of 3 nm and 11 nm/FeOx/ZDS NPs in water or mouse urine are reported in Table 5, along with literature data. The ratio r_2/r_1 is used to classify MRI contrast agents as positive (T_1) or negative (T_2). [60] T_2 contrast agents present a high r_2 and r_2/r_1 (>10) ratio, whereas T_1 contrast agents have low r_2/r_1. The 11 nm/FeOx/ZDS NPs are a T_2 contrast agent (r_2/r_1 = 58 in water and 31 in urine). Previously reported 5 nm FeOx/ZDS also are a T_2 contrast agent, [61] while, 3 nm/FeOx/ZDS NPs are a T_1 contrast agent (r_2/r_1 ratio = 6.1 in water and 6.9 in urine), in line with recent data showing that small iron oxide NPs are T_1 positive contrast agents. [62] Our 3 nm/FeOx/ZDS NPs have relaxivities in water very similar to those displayed by 3 nm ZES-SPIONS [52] provided that allowance is made for the different *B* field. The unequal relaxivities in mouse urine are probably due to the different assay protocols used.

Table 5. Longitudinal (r_1) and transverse (r_2) relaxivity of FeOx/ZDS NPs in water and mouse urine compared to literature data.

		Water			Mouse urine			
NP size / nm	*B* / T	r_1 / $mM^{-1}\ s^{-1}$	r_2 / $mM^{-1}\ s^{-1}$	r_2/r_1	r_1 / $mM^{-1}\ s^{-1}$	r_2 / $mM^{-1}\ s^{-1}$	r_2/r_1	Ref.
3	1.5	5.2	10.5	2.0	–	–	–	[52]
3	4.7	2.36±0.06	14.9±0.1	6.3±0.2	2.16±0.03	14.91±0.08	6.9±0.1	Present work
3	7	1.5	17	11	4.7	9.1	1.9	[52]
5	7	6.1	58.9	9.6	–	–	–	[61]
11	4.7	2.05±0.02	118±4	58±2	2.01±0.04	62±3	31±2	Present work

3.4 Uptake and transport of NPs in phagocytic cells (microglia)

We next assessed how NPs interact with BV2 cells, a microglial cell line of murine origin. [63] Microglial cells are the macrophages resident in the brain and we have chosen them because (i) they are phagocytic cells, expected to effectively internalize NPs and then suited to compare how uptake is affected by the NP physico-chemical properties, and (ii) phagocytic cells offer a transport system for drugs, genes [64] or magnetic NPs in the CNS, where they might externalize NPs in microvesicles.[32]. Cellular iron concentration *C*(Fe), expressed as the cellular iron/protein mass ratio ($\mu g_{Fe}/mg_{protein}$), is tabulated in the Supplementary Data (Tables S1-S5). Corrected ANOVA and Kruskal-Wallis (KW) tests indicated that, in each experiment, not all *C*(Fe) means are equal ($p < 0.05$). The significance of pair-wise *C*(Fe) differences was tested by the post-hoc Conover test adjusted by the Benjamini-Hochberg FDR method (C-BH). In all experiments, the internalized Fe is less than 10% of the Fe initially present as NPs in the culture medium.

The kinetics of the NP uptake by BV2 cells was investigated by treating the cells with reference 11 nm/FeOx/ZDS NPs (50 μg_{Fe}/mL) and measuring *C*(Fe) at different times from treatment, up to 8 h (Figure 4a). *C*(Fe) in BV2 cells increases with the incubation timeand is proportional to the square root of treatment time up to 6 h (Figure S12, Supplementary Data), suggesting that the NP internalization is diffusion-limited. The 6 h and 8 h data are not different ($p = 0.25$). So, the NP uptake reaches a plateau after 6 h and we selected an incubation time of 6 h for further uptake assays.

BV2 cells were exposed to increasing concentrations of 11 nm/FeOx/ZDS NPs from 5 to 500 μg_{Fe}/mL for 6 h to investigate the dose-uptake relationship (Figure 4b). Tthe uptake of reference NPs strongly depends on dose. All mean pairs are different ($p < 0.030$) except for the 25-50 $\mu g_{Fe}/mg_{protein}$ pair ($p = 0.17$). *C*(Fe) depends in an approximately exponential way on the dose of reference NPs, approaching an asymptotic value of (74±7) $\mu g_{Fe}/mg_{protein}$ (Figure S13, Supplementary Data). Similar protein levels were found in lysates obtained from treated and untreated BV2 cells, ruling out NP-dependent cell damage and loss.

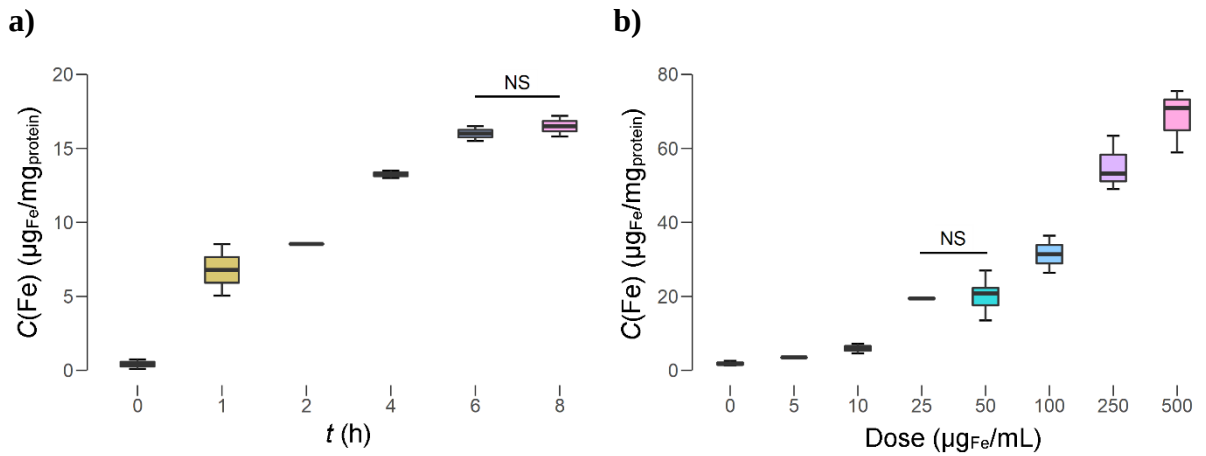

Figure 4. Time- and dose-dependence of the uptake of 11 nm/FeOx/ZDS (reference) NPs by BV2 cells. Cellular iron concentration *C*(Fe) is shown (a) at different times after treatment with NPs (50 μg_{Fe}/mL, $n = 3$), and (b) after treatment with 5 - 500 μg_{Fe}/mL of NPs for 6 h ($n \geq 3$). NS = not significant difference since the post-hoc Conover test adjusted by the Benjamini-Hochberg FDR method was not passed ($p > 0.05$).

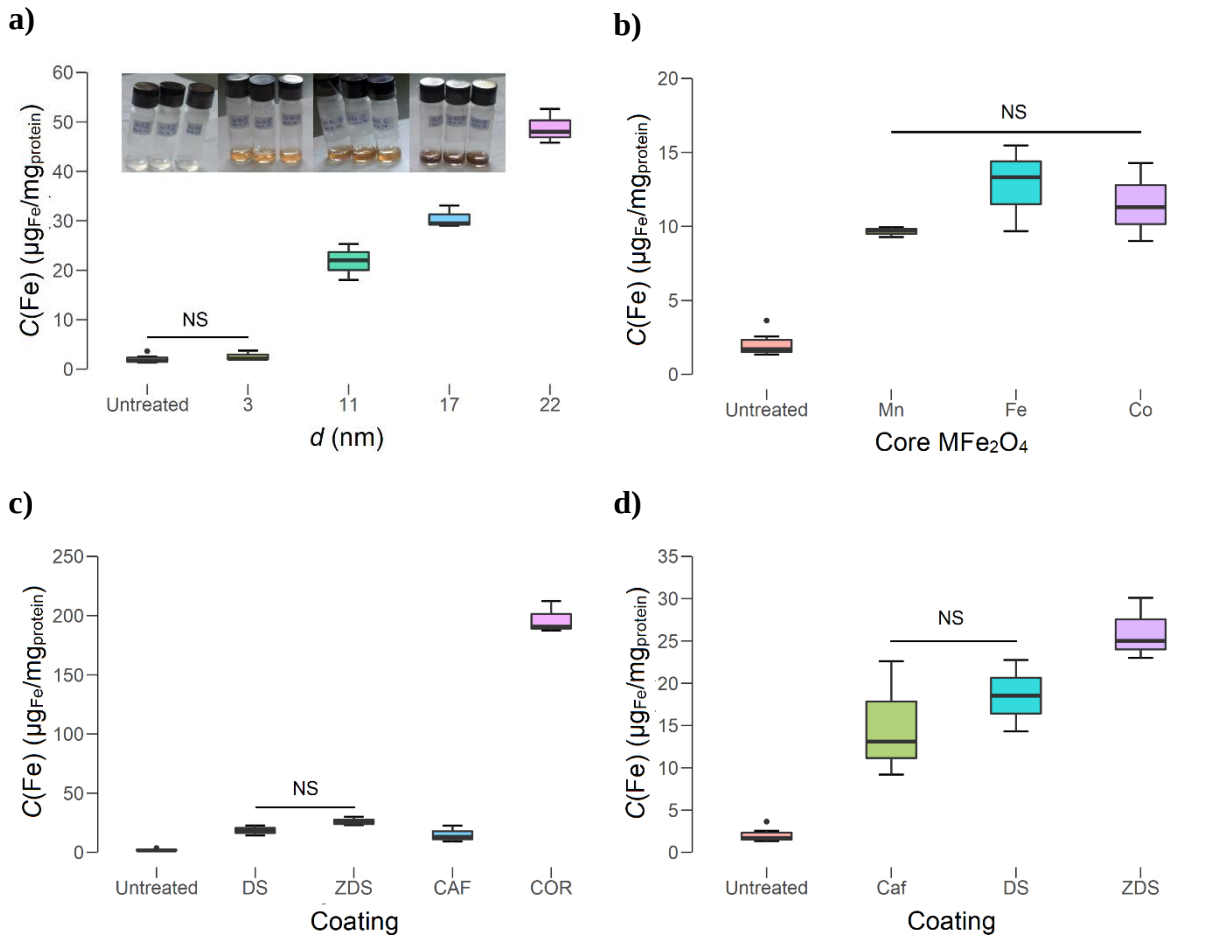

Figure 5. Cellular iron concentration *C*(Fe) in BV2 cells after treatment with NPs differing by core diameter, composition, and coating. a) Treatment with 50 μg_{Fe}/mL of ZDS-coated FeOx NPs with different core diameter for 6 h ($n \geq 3$). The inset shows BV2 cells after treatment with 3, 11, 17, and 22 nm NPs. b) Treatment with 50 μg_{Fe}/mL of ZDS-coated NPs with different composition of the core (MFe_2O_4, M = Mn, Fe, Co) for 6 h ($n \geq 3$); c) Treatment for 6 h with 50 μg_{Fe}/mL of 11 nm FeOx NPs with different coatings (ZDS , DS, CAF, COR; $n \geq 3$). d) Enlargement of c). NS = not significant difference since the post-hoc Conover test adjusted by the Benjamini-Hochberg FDR method was not passed ($p > 0.05$).

When BV2 cells were exposed (50 μg_{Fe}/mL, 6 h) to FeOx/ZDS NPs with different core diameter, the NP uptake showed a marked dependence of the NP size (Figure 5a). All means are different, except for the untreated/3-nm pair ($p = 0.17$). Therefore, BV2 cells do not significantly internalize 3 nm ZDS-coated FeOx NPs. Exposure to larger NPs is associated with a higher *C*(Fe). Since we treated the cells with an equal *mass* of NPs (as opposed to *number* of NPs), *C*(Fe) is proportional to the probability that a NP is internalized. Therefore, larger ZDS-coated FeOx NPs have larger probability to be internalized by BV2 cells, in agreement with theoretical predictions fixing at 50-60 nm the optimal diameter for fast and abundant NP internalization by phagocytic cells.[65, 66]

BV2 cells were exposed to ferrite/ZDS NPs (50 μg_{Fe}/mL for 6 h) to ascertain whether the presence of metals other than iron in the core might affect the NP interaction with microglial cells (Figure 5b). $MnFe_2O_4$ and $CoFe_2O_4$ NPs do not have the same size as the reference FeOx NPs, having diameter 7.4 and 7.1 nm, respectively. The data obtained do not show a correlation between uptake and core composition. All treated cells have *C*(Fe) differing from control but all treated cells have indistinguishable *C*(Fe) ($p = 0.72$ to 1.0). We can conclude that the presence of Mn and Co in the inorganic core does not affect NP internalization, a conclusion not unexpected for densely coated NPs.[23] These results also suggest that the internalization efficiency of 7.1-7.4 nm ZDS-coated ferrite NPs should be similar to that of 11 nm NPs, though a small decrease cannot be completely excluded.

Finally, BV2 cells were treated with ZDS-, DS-, CAF-, and COR-coated 11 nm FeOx NPs for 6 h. (Figure 5c,d). All treated cells have *C*(Fe) differing from control ($p < 0.01$) and the mean uptakes of the treated cells are all different ($p < 0.024$), except that involving DS- and CAF-coated NPs ($p = 0.16$). Treatment with COR-coated NPs led to an increase in *C*(Fe) about 10 times higher than with any other NP type. The large internalization of COR-coated NPs is

due to the aggregated state of the NPs, in line with previous observations.[23] The ZDS-, DS-, and CAF-coated NPs gave similar *C*(Fe) in the 15-26 $\mu g_{Fe}/mg_{protein}$ range. The similarity between DS- and CAF-coated NPs may be due to the close ζ-potential values. The slightly larger internalization of ZDS-coated NPs may again be attributed to the more negative ζ-potential. The chemical difference between the zwitterionic DS and ZDS and the caffeate anion (CAF) coatings seems to be of minor importance with respect to the preferential adsorption of anions that determine the surface potential of the NPs.

In conclusion, phagocytic BV2 cells internalize ZDS-coated NPs in a time- and dose-dependent way. Whereas the core composition and the ligand chemical nature have no influence on the NP uptake, the latter is strongly affected by the NP size to the extent that 3 nm/ZDS/FeOx NPs are not significantly internalized by phagocytic BV2 cells, a promising feature for long-term NP circulation.

Reports on the NP uptake by BV2 cells are not abundant, and in many cases the NP internalization results are not expressed in absolute units so that comparison with the present results is not possible. *C*(Fe) of primary mouse microglia treated for 6 h with FeOx NPs coated with dimercaptosuccinic acid and labeled with BODIPY [d = 5-20 nm, D = 140-160 nm, ζ = (-10)-(-8) mV] [67, 68] was larger than that presently measured for 11 nm/ZDS/FeOx NPs at all doses and similar to that of 22 nm/ZDS/FeOx NPs at the 50 μg_{Fe}/mL dose. (Figure S14, Supplementary Data). *C*(Fe) of the human liver carcinoma cell line HepG2 treated with 9 nm/FeOx/ZDS NPs (D = 12 nm, ζ = –8.6 mV) at a dose of 100 μgFe/mL for 24 h, was 5 $\mu g_{Fe}/mg_{protein}$, [23] much smaller than that in BV2 cells (55 $\mu g_{Fe}/mg_{protein}$, 100 μgFe/mL, 6 h). As expected, phagocytic BV2 cells internalize more ZDS-coated FeOx NPs than non-phagocytic cells. It has been reported that CAF-coated FeOx NPs (d = 9.6 nm, D = 17 nm, ζ = -45 mV) are internalized by U87-MG glioblastoma cells in dose- and time-dependent manner but quantitative data are not available.[55] At the best of our knowledge, internalization data of DS- and COR-coated FeOx/NPs by microglial cells are not present in the literature.

Considering the promising application of magnetic NPs to image and monitor macrophages,[69] we wondered if our NPs could be used to this end. We observed a good correlation between the number of BV2 cells labeled with 11 nm/FeOx/ZDS NPs and the grey-scale value in the MR T_2-weighted images. (Figure S15, Supplementary Data). In the images, the grey difference can be easily identified by the naked eye at cellular density ≥ 10^5 cells/mL.

Having studied the internalization of NPs, we wondered whether intracellular iron is retained by microglial cells after uptake. To address this point, we shifted from immortalized BV2 cells to rat microglia in primary cultures since, at variance from BV2 cells, primary

microglial cells do not significantly proliferate and allow one to assess the maintenance of intracellular iron over a period of days. Primary microglial phagocytes were incubated with 50 μg_{Fe}/mL of 11 nm/ZDS/FeOx NPs for 6 h. At the end of treatment, cells were extensively washed and stained by Prussian blue either immediately or after additional 16-42 h in culture. Virtually all primary cells were positive for the dye at the end of NPs exposure, revealing that ZDS-coated NPs are efficiently internalized by these cells (Figure 6).

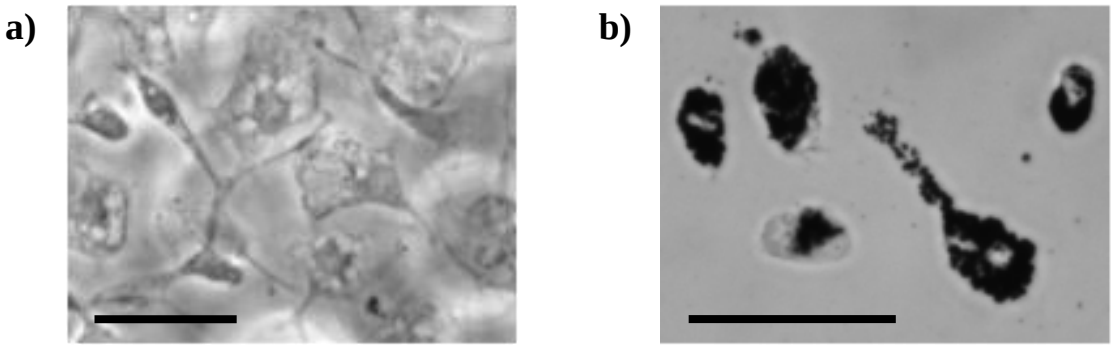

Figure 6. Cytochemical staining of iron in rat primary microglial cells. a) Untreated control cells; b)cells treated with 11 nm/ZDS/FeOx NPs (50 μg_{Fe}/mL) for 6 h. Calibrations bars: 50 μm.

Quantification of intracellular iron revealed a higher Fe level in primary microglia (about 80 $\mu g_{Fe}/mg_{protein}$) than in BV2 cells (20 $\mu g_{Fe}/mg_{protein}$). No significant change in the iron content was observed at 24 and 72 h after NP washing, indicating that primary microglia retained NP iron over time (Figure 7). Evaluation of cellular viability by the propidium iodide/calcein assay showed no significant increase in the percentage of dead cells at different time points of the experiment, excluding acute and delayed NP toxicity (Figure 7, right).

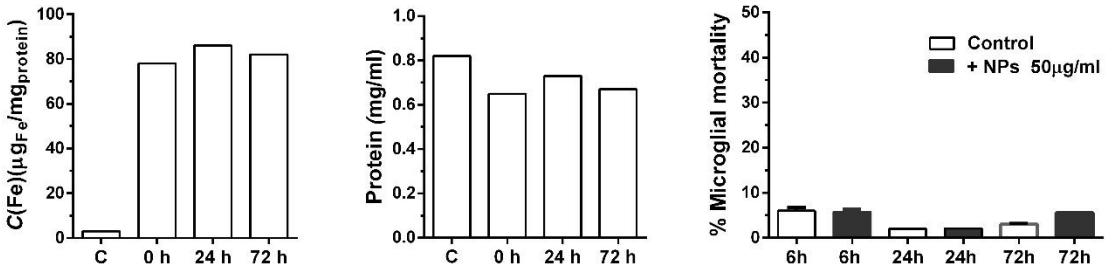

Figure 7. Stability of intracellular iron in rat primary microglia treated with 11 nm/ZDS/FeOx NPs (50 μg_{Fe}/mL). Left: iron content in microglia exposed to NPs for 6 h, washed and lysed at 0, 24 or 72 h after washing compared to untreated microglia (C), (n = 1). Middle: protein quantification of untreated and NP-treated microglia, lysed at 0, 24 or 72 h after NP washout (n = 1). Right: mortality of untreated (white columns) and NP-treated (black columns) microglia at 0, 24 or 72 h after NP washout (n = 3).

It has been recently showed that THP-1 cells are able to release extracellular vesicles (EVs), which contain iron oxide [32]. Since microglial cells are the resident CNS macrophages, this opens the possibility that NPs may be transferred between microglial cells via EVs. To address this possibility microglial cells were treated with 11 nm/ZDS/FeOx NPs (50 μg_{Fe}/mL) for 6 h and extensively washed. Fluorescent microglial cells, stained with the membrane dye PKH67, were then plated on top of NP-treated microglia and co-cultured for 24 hr. The cells were fixed and stained with Prussian Blue to visualize intracellular iron deposits. Iron accumulation was detected in 86% of PKH67-labeled microglial cells, indicating that iron very efficiently shuttles in microglia (Figure 8).

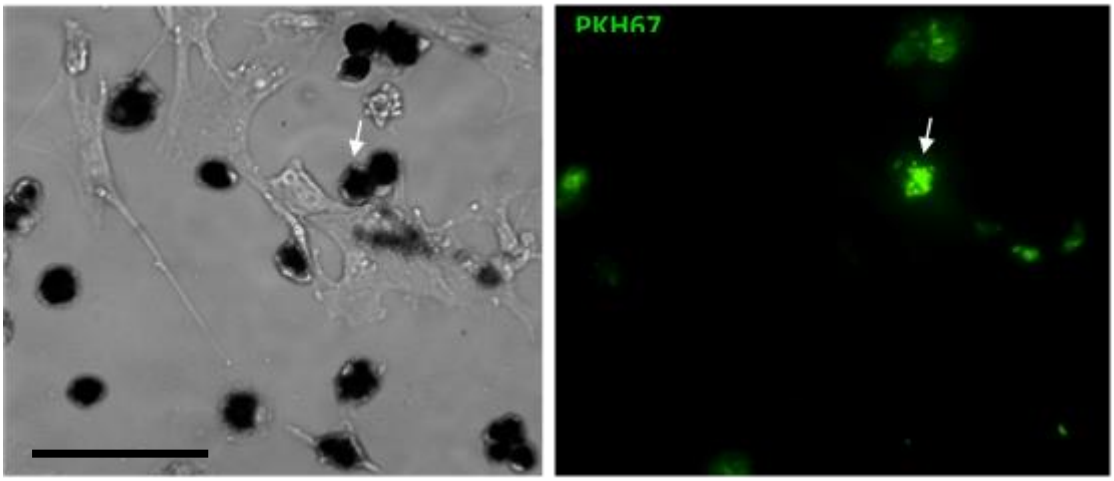

Figure 8. Cell-to-cell iron shuttling. Primary microglial cells were treated with 11 nm/ZDS/FeOx NPs (50 μg_{Fe}/mL) for 6 h washed, co-cultured with PKH67 positive microglia for 24 h, fixed and stained with Prussian Blue. DIC image shows iron accumulations in most microglial cells (left). Fluorescent image (right) shows intracellular iron inside PKH67 (green) positive cells (arrow), indicating iron transfer from PKH67 negative to PKH67 positive cells. Calibration bar: 50 µm.

The transfer of iron is paralleled by the transfer of fluorescent vesicular structures, suggesting that EV production and uptake in recipient cells may underlie shuttling of iron between cultured microglia (Figure 9). Further work is required to characterize iron content in EVs and confirm this hypothesis.

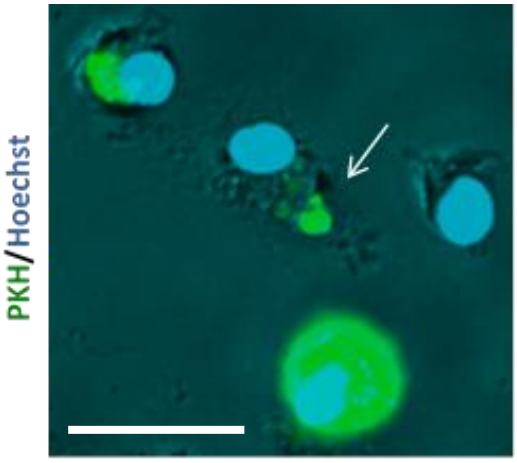

Figure 9. Cell-to-cell shuttling of EVs. Primary microglial cells stained with PKH67 (green) were plated on control microglia and maintained co-cultures for 24 h. Cells were fixed and their

nuclei stained with Hoechst (light blue). Merge between DIC and fluorescent images shows the presence of green vesicles inside a PKH67 negative microglia (arrow). Calibration bar: 20 µm.

3.5 Immune/inflammation-related effects of ligand-exchanged NPs

3.5.1 Endotoxin contamination of NPs.

Before running any biological assay, it was important to assess whether NPs are unintentionally contaminated with bacterial endotoxin, since immune responses are easily triggered even by minute amounts of it. [70] Indeed, in the absence of endotoxin, the immune-activating effects of several NPs can no longer be observed.[71] As endotoxin contamination is difficult to eliminate,[72] the best way of avoiding it is to run NP synthesis in endotoxin-free conditions.[73] Endotoxin levels were assessed by a modified protocol, adapted for NPs, using a selected commercial LAL assay.[48] As shown in TableS6 (Supplementary data), some of the NPs had a significant contamination, while others were much cleaner, and in others the contamination could not be measured.

We used the NPs at concentrations such that the endotoxin contamination was below 0.1 EU/mL and no interference in the LPS recovery test occurred. [48]

3.5.2 NPs do not activate an innate/inflammatory reaction in human blood cells.

To assess whether NPs have the capacity of triggering an innate immune reaction in human cells, we have used a very effective assay that describes the overall effect of all blood cells, the whole blood assay (WBA), which is one of the assay recommended for pyrogen and endotoxin testing.[74, 75] We have focused on the ability of NPs to induce the production of two inflammation-related cytokines, the inflammatory factor IL-1β and its natural inhibitor IL-1Ra. Both factors are mainly produced by monocytes, the major innate immune cells present in the blood, thus this assay essentially reproduces the results of other assays, the PBMC activation assay and the monocyte activation test (MAT), also recommended as suitable tests for endotoxin detection by the European Centre for the Validation of Alternative Methods (ECVAM). As shown in the Figure 10, in unstimulated conditions blood cells typically produce a significant level of the anti-inflammatory cytokine IL-1Ra, but not the inflammatory cytokine IL-1β, this being a homoeostatic behavior. In response to the inflammatory stimulus LPS, blood cells produce a significant level of the innate inflammatory cytokine and, as a feed-back self-

protecting reaction, higher levels of the inhibitor, aiming at controlling the activity of IL-1β. Thus, a proper defensive immune reaction implies the production of the active effectors and the molecules for controlling its activity, so as to allow defense without risking side effects. An anomalous response, with uncontrolled inflammation, would be characterized by high levels of IL-1β not accompanied by high levels of IL-1Ra. None of the different types of NPs, independently of size, core or coating composition, was able to elicit any activation in blood cells, which in the presence of NPs behaved as in the presence of medium alone (negative control) (Figure 10). As a routine procedure when using NPs *in vitro* on human cells, NPs were previously incubated with human plasma (from the same donor as the blood used in the WBA), so as to mimic the *in vivo* conditions of NP administration, in which NPs are expected to be immediately coated with plasma proteins and factors before getting in contact with blood cells. We have tested some of these NPs also in the other two assays, the PBMC activation assay and the MAT, and obtained identical results, *i.e.*, no significant effects were ever detectable (data not shown). Thus, the NPs are unable to directly induce an innate/inflammatory response in human blood cells.

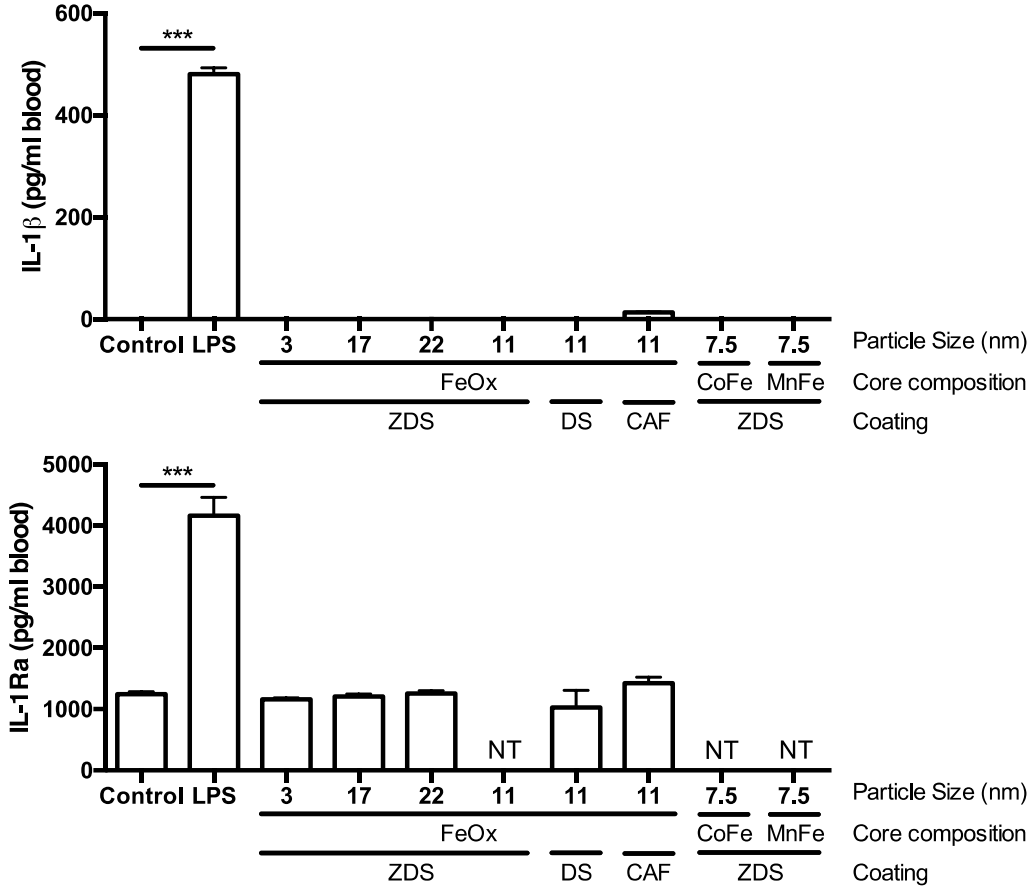

Figure 10. Direct activation-inducing effect of ligand-exchanged NPs on human blood cells. The effect of size, coating, and core composition of NPs in inducing the production of the immune/inflammatory cytokines IL-1β and IL-1Ra in human whole blood is shown. Fresh blood was exposed to medium alone (control) or containing LPS (2.5 ng/mL, positive control), or different types of ligand exchanged NPs for 24 h. *** $p < 0.001$ *vs*. control, NT = not tested. Data are representative of two donors and are reported as mean ± SD (four replicates/donor).

NPs do not interfere with an ongoing human innate/inflammatory reaction.

Although the NPs turned out completely inactive in triggering an immune reaction in human cells, they might nevertheless be able to interfere with an ongoing protective reaction, by either exacerbating or suppressing it, thereby posing a health risk. Thus, we have tested the NPs in a kinetic *in vitro* model that reproduces the course of a defensive innate immune reaction [71] The results in the Figure 11 report the profiles of the defensive reaction, in terms of expression and production of the inflammatory and anti-inflammatory cytokines IL-1β and IL-1Ra by human blood monocytes, in the absence or in the presence of 11 nm/ZDS/FeOx NPs. IL-1β

expression peaks at 4-8 h, whereas the production of the cytokine is maximal at 14 h (as production implies a number of post-transcriptional steps). The presence of these NPs does not affect either expression or production of the inflammatory cytokine (Figure 11, left panels). The inhibitory factor IL-1Ra is expressed later relative to IL-1 (peaking at 15 h), but the protein is released immediately, as there are no post-transcriptional steps. This makes the peak of IL-1 production coinciding with the peak of the inhibitor, thereby obtaining the perfect balance between activity and its control. Also, in the case of IL-1Ra, the presence of the NPs does not affect the expression or production of the inhibitor (Figure 11, right panels), except for a slightly higher production of the anti-inflammatory factor at 24 h in the NP-treated group. This profile implies that the balance between inflammation and anti-inflammation is well maintained also in the presence of NPs. Tests with other NPs showed the same behavior (data not shown).

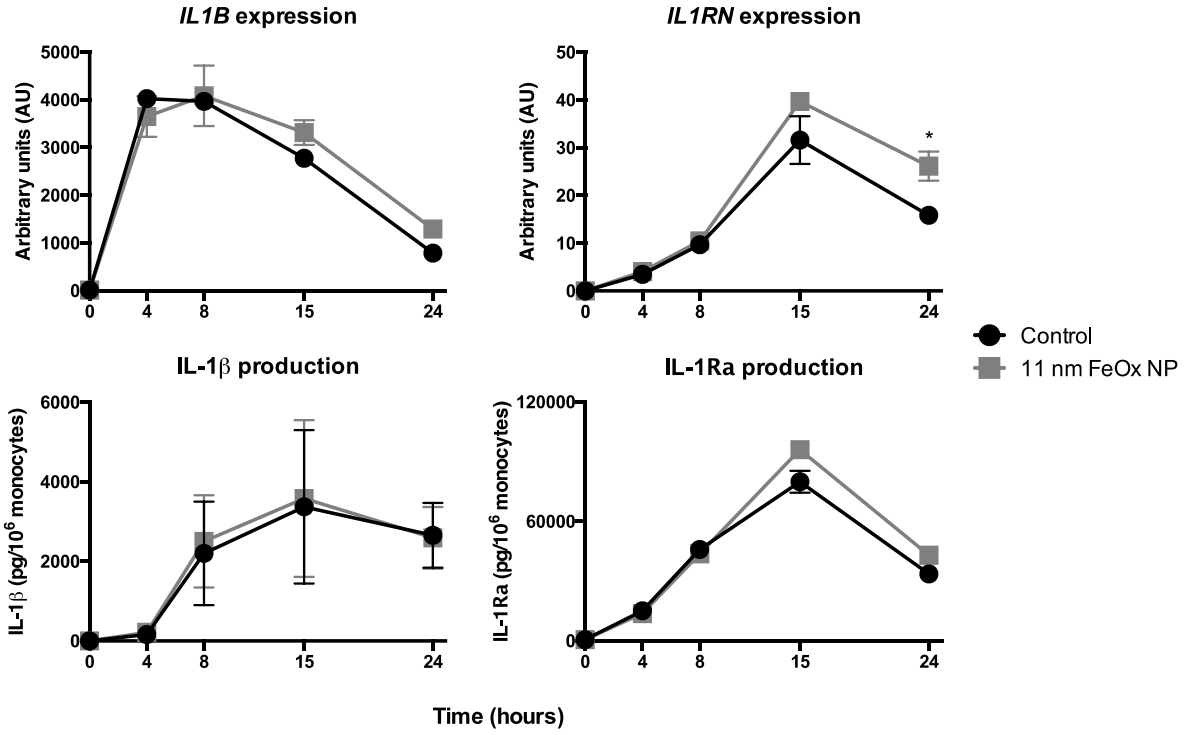

Figure 11. Influence of NPs on the course of a defensive immune innate/inflammatory response. Human blood monocytes were exposed to a sequence of treatments simulating a normal inflammatory response (see Experimental Section). Control (circles) and NP treatment (squares) samples were assessed at different time points. Representative data (mean ± SD) from 2-4 replicate tests from 1 representative donor (IL-1Ra) or average of 2 donors (IL-1β). Gene expression of *IL1B* and *IL1RN* (upper panels), the genes encoding IL-1β and IL-1Ra, is shown

as arbitrary units (AU). Cytokine production (lower panels) is expressed as pg/10^6 monocytes. * $p < 0.05$ *vs*. control.

The conclusion is that, at the endotoxin-free concentrations used, none of the investigated NPs has a direct effect in eliciting an innate immune/inflammatory reaction in human blood cells, and in addition they do not interfere with the normal development of a defensive reaction, and can therefore be considered as immunologically safe. These findings may seem at variance with the immune stimulatory or suppressive effects described for several types of polymer-coated FeOx NPs reported in Ref. [5], with the caveat that many of the previous studies were performed with very high dosages in mice or *in vitro* on tumor cell lines, and that endotoxin contamination was usually not assessed..

3.6 Biodistribution of ZDS/FeOx NPs in mice

In vivo MRI characterization study revealed that both 3 and 11 nm/FeOx/ZDS NPs are in part quickly (≈1 h) cleared from the blood through the kidneys and in part remain in the mononuclear phagocyte system (MPS), *e.g.*, in the liver and spleen, for prolonged periods of time. This behavior is clearly seen in the T_2-weighted MR images and in the time courses analysis of the T_2* signal intensity (SI) (Figures 12 and 13). However, the 3 and 11 nm iron oxide NPs have a slightly different biokinetic behavior and distribution.

Figures 12, 13 and 14 show transverse and coronal views of the abdomen of representative mice for each group of treatment before and at different time points after injection. As shown by the analysis of T_2* SI (Figures 12 and 13), we found considerable similarity between animals within each experimental group.

The T_2* SI of dorsal muscle did not significantly change after 3 and 11 nm/FeOx/ZDS NPs injection, showing that a negligible amount of NPs is present in dorsal muscle (Figure S16, Supplementary Data).

On the contrary, in the MPS of liver and spleen, the T_2* SI changed rapidly. As shown in Figure 12, the liver darkened just after injection, due to the early hepatic uptake of NPs. The NP accumulation depends on both dose and size. KW analysis demonstrates that both 3 nm and 11 nm/FeOx/ZDS NP injections significantly affected the T_2* SI of liver overtime ($p < 0.05$ for 4 mg/kg of 3 nm/FeOx/ZDS NPs, and $p < 0.01$ for 1 mg/kg of 11 nm/FeOx/ZDS NPs, respectively). The T_2* SI fell by about 10% and 65% at 1 h after injection of the 3

nm/FeOx/ZDS NPs for the dose 1 and 4 mg/kg, respectively, and the T_2* SI reduction was still appreciable at 6 h. This effect was larger for the 11 nm/FeOx/ZDS NPs. The T_2* SI fell by about 30% and 80% within 1-4 h after NP injection for the dose 1 and 4 mg/kg, respectively. The T_2* SI was still significantly lower than the baseline at 1 day ($p < 0.05$ by Dunnett's Multiple Comparison post-hoc test, DMC) and then increased over time from day 2 and reached values similar to the baseline at day 14 (Figure 12). There is evidence that long-term clearance of FeOx NPs trapped in MPS organs occur through the feces. [76]

In the spleen, the T_2* SI decreased by 30-40 at 15 minutes after 1 and 4 mg/kg of 3 nm/FeOx/ZDS NP injection but it was only about 20-40% at 6 h. For the 11 nm/FeOx/ZDS NPs, the change of T_2* SI was about 40 and 80% at 15 minutes after 1 and 4 mg/kg NP injection, respectively, and slowly recovered, remaining low until day 14. These data show that the clearance of FeOx/ZDS NPs from the MPS depends on both NP size and organ, and that it is faster in the liver than in the spleen for the 11 nm NPs and the opposite for the 3 nm NPs.

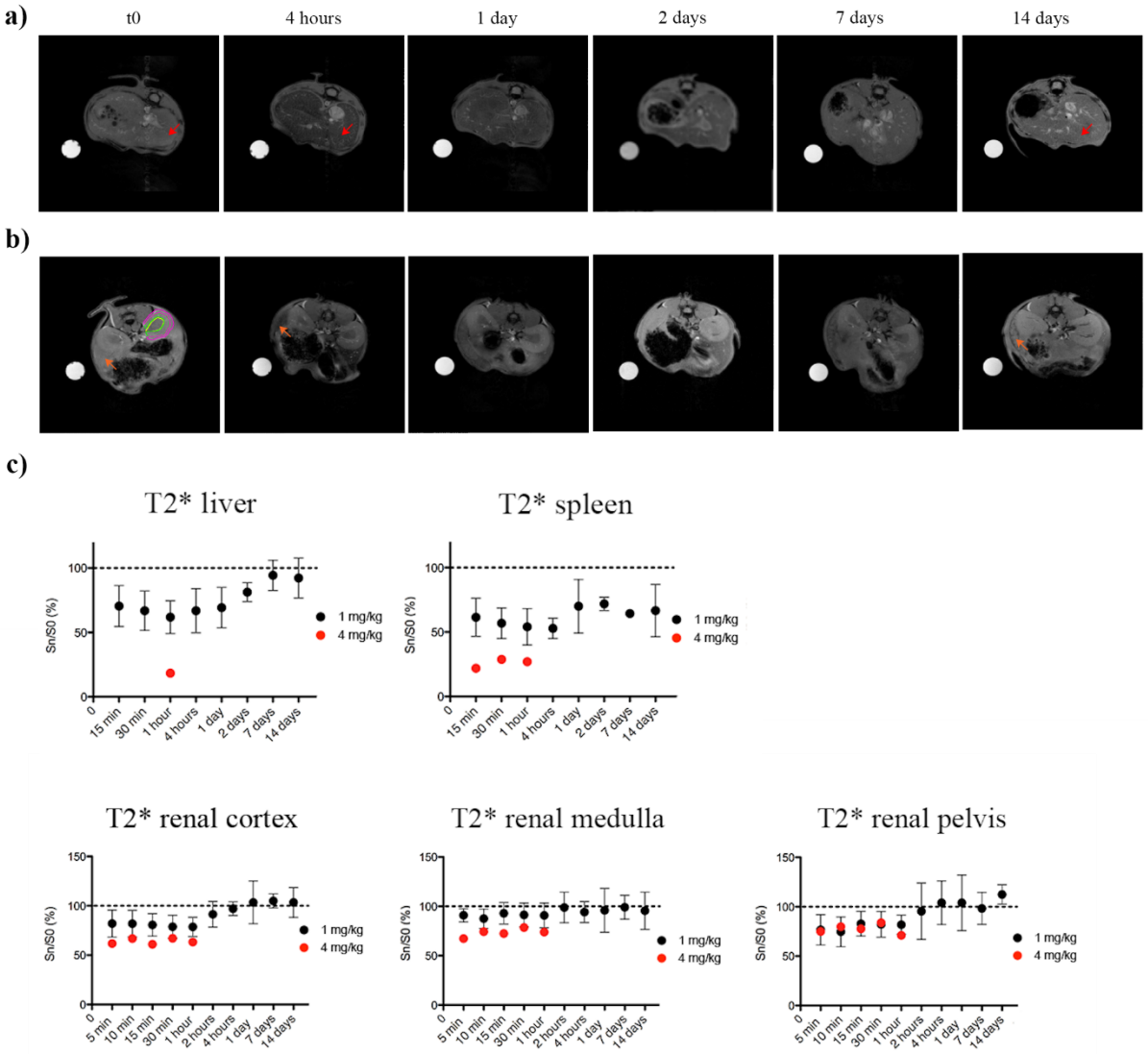

Figure 12. Representative transverse T_2-weighted MR images of liver (a), spleen and kidney (b) in a mouse injected with 1 mg/kg of 11 nm/FeOx/ZDS NPs, acquired before (t_0) and at different time points after NP injection. The arrows indicate liver (red) and spleen (orange), whereas outlines indicate borders of the renal cortex (purple), medulla (green) and pelvis (yellow). (c) Graphs of the T_2* SI expressed as percent of pre-injection baseline and after normalization of each value with corresponding signal produced by the $CuSO_4$ phantom (n = 5 mice for 1 mg/kg of 11 nm/FeOx/ZDS NPs; n = 1 mouse for 4 mg/kg of 11 nm/FeOx/ZDS NPs). KW analysis demonstrated that the NP injection significantly affected the T_2 value in liver ($p < 0.01$), spleen ($p < 0.01$) renal cortex ($p < 0.01$) and renal pelvis ($p < 0.01$). ** $p < 0.01$ and * $p < 0.05$ vs. t_0 by DMC post hoc test.

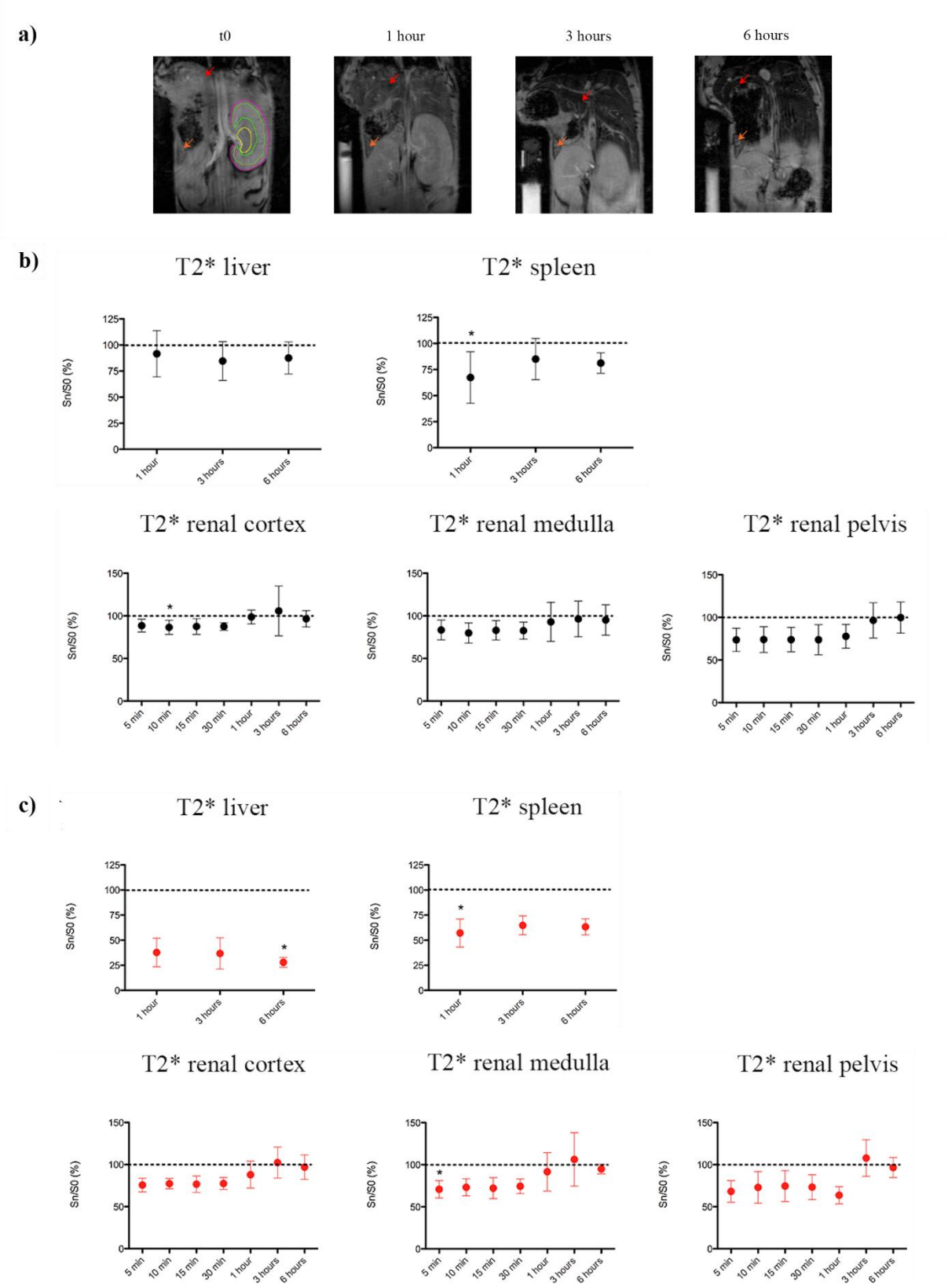

Figure 13. Representative coronal T_2-weighted MR images of liver, spleen and kidney (a) in a mouse injected with 4 mg_{Fe}/kg of 3 nm/FeOx/ZDS NPs, acquired before (t_0) and at different time points after NP injection. The arrows indicate liver (red) and spleen (orange), whereas outlines indicate borders of the renal cortex (purple), medulla (green) and pelvis (yellow).

Graphs (b, c) of the T_2* SI of different organs, expressed as percent of pre-injection baseline and after normalization of each value by the corresponding signal produced by the $CuSO_4$ phantom. b) 1 mg_{Fe}/kg (n = 5 mice); c) 4 mg_{Fe}/kg (n = 5 mice). KW analysis demonstrated that the NP injection significantly affected the T_2 value in liver ($p < 0.05$ only for dose of 4 mg/kg), spleen ($p < 0.05$) renal cortex ($p < 0.05$), renal medulla ($p < 0.05$ only for dose of 4 mg/kg) and renal pelvis ($p < 0.05$). * $p < 0.05$ vs. t_0 by DMC post hoc test.

To assess renal clearance, we investigated the T_2* SI in the different parts of the kidney and in the bladder. The T_2* SI in the renal cortex and medulla slightly fell in NP dose and size dependent manner (Figures 12 and 13). In the renal cortex, the T_2* SI fell by about 10% and 20% at 5 minutes after 1 mg/kg of 3 and 11 nm/FeOx/ZDS NPs, respectively. For the 4 mg/kg dose of 3 and 11 nm/FeOx/ZDS NPs, the decrease was about 25% and 40%, respectively. The T_2* SI returned to the baseline level within 1 h, except for 11 nm/FeOx/ZDS NPs. In the latter case, the T_2* SI reduction was still appreciable at 2 h, but the value of T_2* SI was comparable to the baseline at 4 h. In the renal medulla the kinetic behavior of T_2* SI is similar. The T_2* SI fell by about 30-35% at 5 minutes after 4 mg/kg of 3 and 11 nm/FeOx/ZDS NPs and returned to baseline level after 2 h from NP injection. Similar results were obtained for the renal pelvis. Both 3 and 11 nm/FeOx/ZDS NPs rapidly (≈1 h) clear through the kidney. No sign of NP accumulation was detected.

This conclusion is further supported by the bright signal appearing early within the bladder, indicating the excretion of urine containing NPs. Figure 14 shows that, 5 min after injection, the bladder displays some positive contrast (white signal) that increases and extends in the bladder overtime, up to 1 h. This indicates excretion of both 3 and 11 nm/FeOx/ZDS NPs.

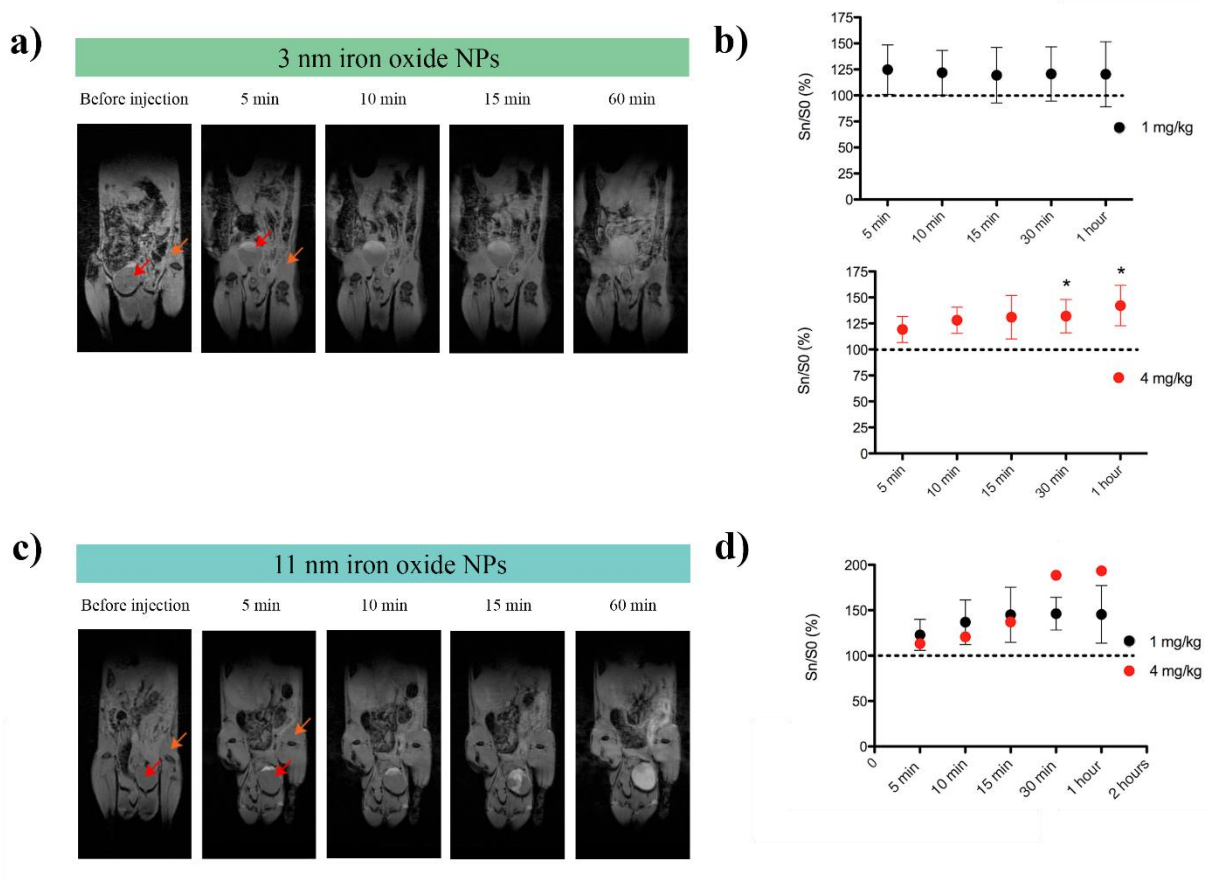

Figure 14. Representative coronal T_2-weighted MR images of a mouse injected with 1 mg/kg of 3 nm/FeOx/ZDS NPs (a) or 11 nm/FeOx/ZDS NPs (c), acquired before (t_0) and at different time points after NP injection. The arrows indicate bladder (red) and muscle (orange). Graphs of the bladder T_2* SI are expressed as percent of pre-injection baseline after normalization of each value by the corresponding signal produced by the $CuSO_4$ phantom [(b) n = 4 mice for 1 and 4 mg/kg of 3 nm/FeOx/ZDS NPs; (d) n = 3 mice for 1 mg/kg of 11 nm/FeOx/ZDS NPs and n = 1 mouse for 4 mg/kg of 11 nm/FeOx/ZDS NPs]. KW analysis demonstrates that 4 mg/kg of 3 nm/FeOx/ZDS NPs injection significantly affected T_2* SI of urine ($p < 0.05$). * $p < 0.05$ vs. t_0 by DMC post hoc test.

To further characterize *in vivo* the MR contrast effects of the NPs, we also evaluated T_2 relaxation times derived from MR images. The T_2 relaxation times graphed in Figure 15 and the corresponding MR images show that 11 nm/FeOx/ZDS NPs determined a relevant enhancement of the liver and spleen contrast overtime (One-way ANOVA, $p < 0.05$ and $p < 0.01$, respectively). Changes in T_2 were still induced at 4 h post-injection and the contrast enhancement effect produced by NPs was found to persist in the days following injection. In

the liver, the contrast enhancement effect was lost within 7 days, whereas it was still present in the spleen after 14 days, confirming the different clearance of the NPs from these organs observed in T_2-weighted images. At renal level, we did not observe any significant change in the T_2 value overtime in the three regions analyzed (cortex, medulla and pelvis). These results confirm the conclusions drawn from the analysis of the T_2*.

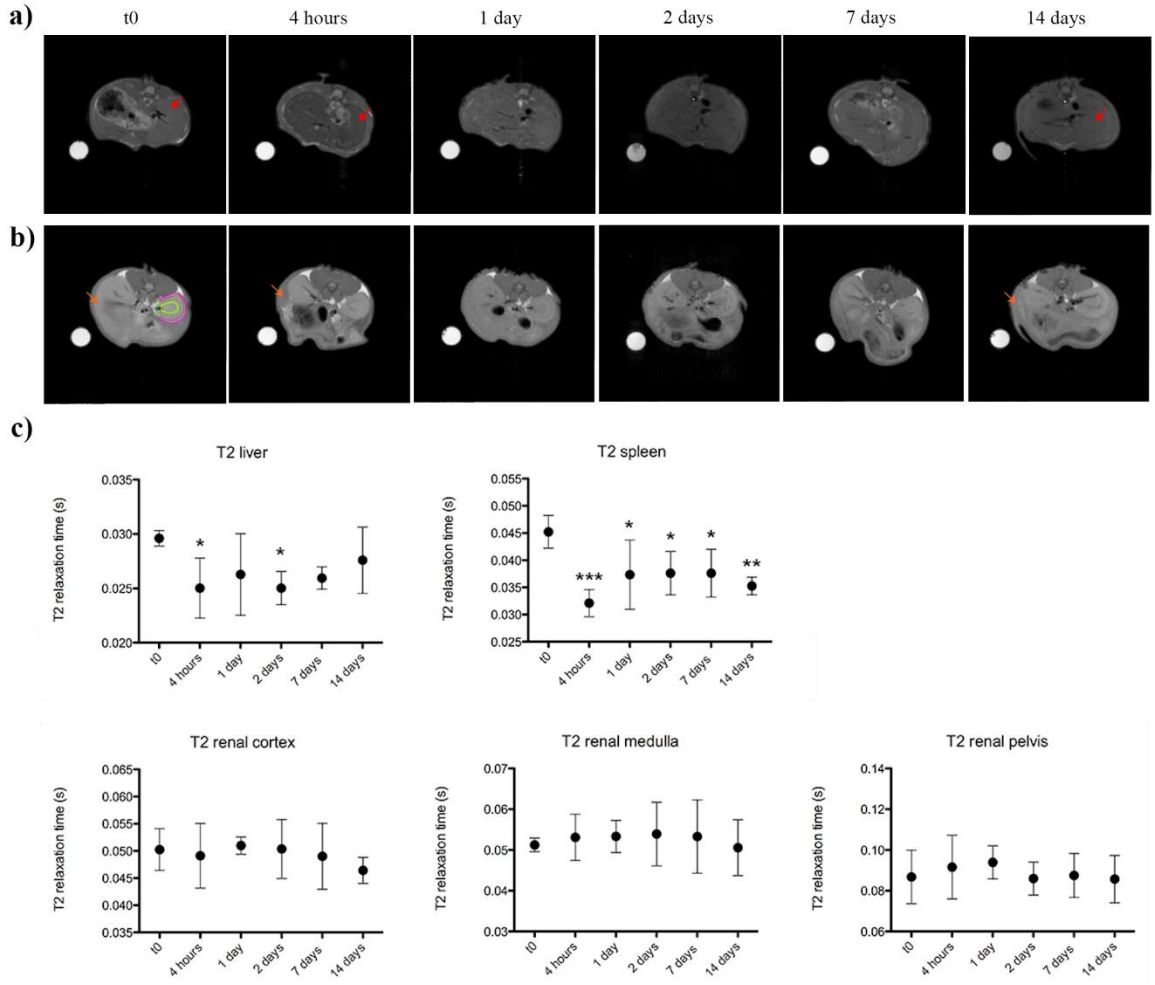

Figure 15. Representative transverse T_2 MAP MR images of liver (a), spleen and kidney (b) in a mouse injected with 1 mg/kg of 11 nm/FeOx/ZDS NPs, acquired before (t_0) and at different time points after NP injection. The arrows indicate liver (red) and spleen (orange), whereas outlines indicate borders of the renal cortex (purple), medulla (green) and pelvis (yellow). (c) Evolution of the T_2 relaxation times. One-way ANOVA analysis demonstrates that NPs injection significantly affected T_2 value in liver ($p < 0.05$) and spleen ($p < 0.01$). *** $p < 0.001$, ** $p < 0.01$ and * $p < 0.05$ vs. t_0 by Dunnett's post hoc test.

After the last MRI acquisition, mice were sacrificed and paraffin-embedded sections of liver, kidney and dorsal muscle were histologically stained for iron (Figure 16). In the liver, Prussian Blue staining revealed positive stained granules, indicating iron accumulation, in Kupffer cells and some hepatic sinusoids 4 h after injection with NPs. The iron staining appeared to be NP dose and size dependent. The iron accumulation was higher for higher dose of NPs and for 11 nm NPs with respect to 3 nm NPs (data not shown). At 14 days after NP injection, no blue-stained iron particles were detected in the liver. Conversely, we observed an increased accumulation of blue granules in the spleen of mice treated with 11 nm/FeOx/ZDS NPs compared to control mice (treated with physiological solution) at day 14 after injection. In the spleen, the iron deposition was consistently intracellular, mainly in red pulp areas, suggesting that the NPs had accumulated in macrophages. Iron was never detected in kidney and dorsal muscle of treated mice at any time point. No stained granules were detected in any tissue of control mice (treated with physiological solution). The correlation between T_2* SI and the histological results confirms that NPs accumulate in liver and spleen but not in kidneys despite their transit through the urinary tract.

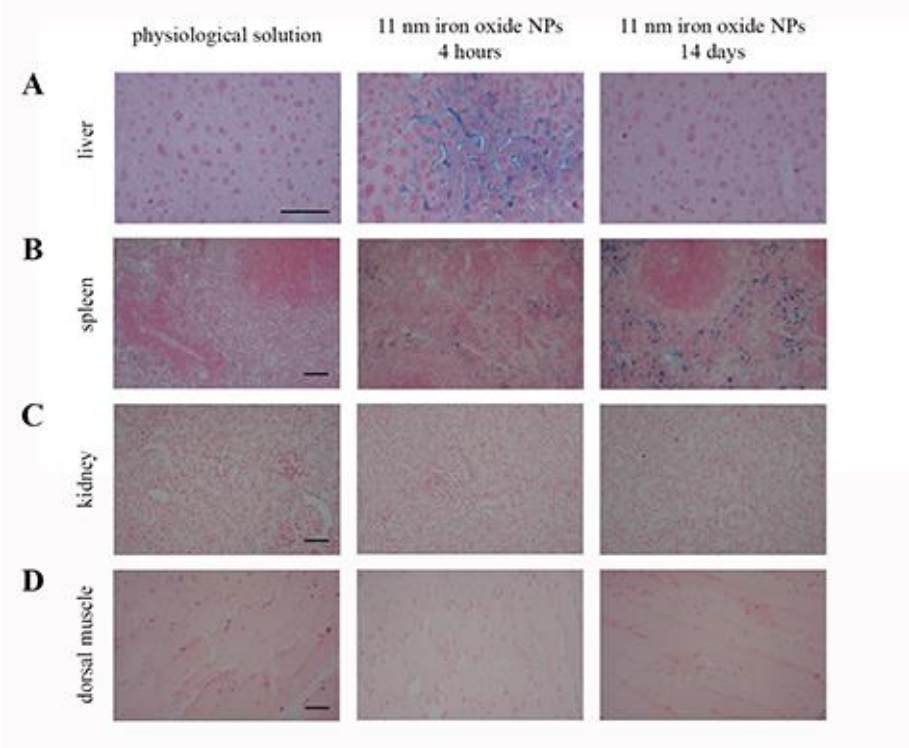

Figure 16. Representative Prussian blue staining of liver (A), spleen (B), kidney (C) and dorsal muscle (D) of mice injected with physiological solution (left panels) or 1 mg/kg of 11 nm/FeOx/ZDS NPs at 4 h (middle panels) and 14 days (right panels) after injection. Scale bar: 50 μm.

Renal clearance of NPs substantially reduces the NP toxicity by reducing NP accumulation in the body.[35] Renal excretion occurs when the NPs are able to pass through the renal glomerular filtration barrier (GFB), which is composed of three layers (Figure S17, Supplementary Data). Going from the capillary space to the urinary space, these are (*i*) the glycocalyx-coated fenestrated capillary endothelium, (*ii*) the glomerular basal membrane (GBM), and (*iii*) the podocyte visceral epithelium. Current models suggest that all three layers of the filtration barrier are likely important (including the glycocalyx of the endothelial layer), but relative contributions remain unknown.[77]

Using cysteine-coated zwitterionic CdSe/ZnS quantum dots, it was established that inorganic NPs with hydrodynamic diameter $D \leq 5.5$ nm are cleared through the kidneys of healthy rats,[19] a size cutoff similar to the accepted 6-nm limit for proteins.[78] Many subsequent reports showed renal clearance of NPs with $D \lessapprox 6$ nm, [35] including ZDS-coated FeOx NPs.[52, 61] This cutoff for inorganic NPs has been held as valid up to now.

The rapid renal excretion of our 3 nm/FeOx/ZDS NPs is not unexpected since it has been previously reported for similar NPs, having core diameter $d \approx 3$ nm, $D = 4.4/4.7$ nm [52] and $d = 4.8$ nm, $D = 6.5$ nm.[61] These values place our 3 nm/FeOx/ZDS NPs ($d = 3.2$ nm, $D = 9$ nm) somewhat beyond the established cutoff for D but, considered the relatively large uncertainty of D and the small core size d, the renal clearance of our NPs seems in line with previous results. Conversely, it is surprising that 11 nm/FeOx/ZDS NPs are in part quickly excreted since *both* $d = 10.7$ nm and $D = (13 \pm 1)$ nm are well beyond the accepted threshold for renal clearance. The higher cutoff of FeOx/ZDS NPs with respect to CdSe/ZnS/cysteine quantum dots shows that the nature of the particles affects their renal filterability. Assuming that the cutoff difference is related to the organic coating (and not to the inorganic core), the different filterability should be ascribed to the unequal interactions of the carboxybetaine amino acid cysteine ($–NH_3^+/–COO^-$) and sulfobetaine ZDS ($>NMe_2^+/–SO_3^-$) with the GFB barrier. This conclusion is supported by functional studies that showed that the size cutoff for macromolecules depend on their chemical structure.[79]

The renal glomerulus structure is not inconsistent with the excretion of NPs having d = 10.7 nm and D = 13 nm. Recent imaging studies have shown that the GFB pore sizes are larger and more polydisperse than previously thought. The glomerular capillary endothelium of rats contains pores (fenestrae) with diameter 74 ± 15 nm [80] and in humans the pores have size 70-100 nm.[81] The glycocalyx covering the luminal side of the endothelium is loose [82] and the spacing of its fibers in rats is at least 20 nm. [83] The GBM is a meshwork of proteoglycan fibers having pores in the 10-32 nm range in rats.[84] Finally, the filtration slits between the epithelial podocytes are about 40 nm wide in mice. [85] In rats, the proteins bridging across the slits [86] form pores with size 12 ± 1 nm (range: 6 to 30 nm) when observed by scanning electron microscopy [87] and size 22 ± 8 nm when observed by helium ion scanning microscopy.[80] Therefore, there are no obvious structural limits to the excretion of NPs with D > 5.5 nm.

4. Conclusions

ZDS-coated medium-size (10-11 nm) FeOx NPs are promising nano-scaffolds as they do not adsorb serum proteins and display low internalization by non-phagocytic cells.[21, 23] We have further supported the innocence of these NPs by showing that they (i) do not activate nor interfere with the human innate/inflammatory reactions and (ii) are scarcely internalized also by phagocytic (BV2) cells.

To broaden the search for innocent nano-scaffolds, we synthesized eight types of magnetic NPs, each differing from the reference NPs for a single feature, namely, size, core composition, and coating. Except for COR-coated NPs, all are colloidally stable in aqueous media and do not adsorb serum proteins *in vitro*. The NP uptake only depends on the NP size. The NPs are immunologically safe, an indispensable pre-requisite for medical applications in humans. Therefore, all colloidally-stable NP types are innocent scaffolds and, within the investigated range, the most convenient NP type can be used. For instance, usage of DS instead of ZDS avoids the protection/deprotection of the phenolic hydroxyls during the methylation of the amine group. Synthetic convenience is highest using commercially available CAF.

The coating ligand has scarce influence on the NP uptake. This does not question the known dependence of NP internalization on surface charge [88] but is related to the unexpected result that our NP types have negative ζ potential. The effective surface charge of NPs coated with small (zwitter)ionic molecules is determined by the preferential adsorption of anions and

not by the formal (possibly pH-dependent) ligand charge. This must be taken into account when designing NPs for biomedical applications.

Both small (3 nm) and medium-size (11 nm) ZDS/FeOx NPs are promising MRI contrast agents (of T_1 and T_2 type, respectively) because of their good relaxivity and bio-distribution. Despite some accumulation in spleen and kidney lasting about 2 weeks, both are rapidly (≈1 h) excreted through the urinary system. The renal clearance of 3 nm/FeOx/ZDS NPs has already been proved [52] but that of 11 nm/FeOx/ZDS is surprising because they are much larger than the established size threshold for renal clearance. This finding shows that the 6 nm threshold cannot be generalized as it may depend on the chemical nature of the circulating particles. Renal filterability of zwitterionic FeOx NPs with D up to 13 nm (and d = 10.7 nm) broadens the pathway to effective theranostic systems based on magnetic NPs since such medium-sized FeOx NPs have much larger magnetic moment than typical ultrasmall FeOx NPs (50-fold increase from 3 to 11 nm), leading to better T_2 relaxivity,[89] specific absorption ratio for hyperthermia,[90] and response to external magnetic fields.[91]

Some issues have yet to be clarified. The hypothesis that NPs may induce innate immune memory by epigenetic modulation of gene expression is important from the translation standpoint and requires careful scrutiny. [92] Another important issue is the quantitation of the fraction of NPs that are renally excreted, captured by the MPS NPs, or accumulated in other compartments. Finally, a detailed investigation of the *in vivo* interaction between NPs and the liver [93, 94] and spleen will be instrumental to design NPs with minimal accumulation in these organs.

Acknowledgments

Financial support by Fondazione CARIPLO (Milano, Italy) under grant no. 2011-2114 is gratefully acknowledged. DB, PI, YL and BJS were also supported by the EU projects NanoTOES (FP7 PITN-GA-2010-264506), PANDORA (H2020 GA 611881), and ENDONANO (H2020 GA 812661).

Appendix A. Supplementary Data

Electron diffraction patterns, additional TEM images, and NP diameter distributions. Infrared, electron energy loss (EELS), and energy dispersive X-Ray (EDX) spectra; electron spectroscopy imaging maps. Intensity of light scattered as a function of time. ζ

potential at different pH. Relaxometry of FeOx/ZDS NPs. Procedures for the synthesis of Fe(III) oleate, dopamine sulfonate, zwitterionic dopamine sulfonate, coryneine chloride. Quantification method, tabulated data, fit to quantitative models, and comparison to literature data for the internalization of NPs by microglial cells. Proof that the internalized mass of NP iron is proportional to NP internalization efficiency. Detectability of NP-labeled BV-2 cells by MRI. Endotoxin contamination of the nanoparticles. T_2^* signal intensity of dorsal muscle of NP-treated mice. Schematic picture of the renal glomerular filtration barrier.

References

[1] C.L. Ventola, Progress in Nanomedicine: Approved and Investigational Nanodrugs, P & T : a peer-reviewed journal for formulary management 42(12) (2017) 742-755.
[2] Y.H. Choi, H.-K. Han, Nanomedicines: current status and future perspectives in aspect of drug delivery and pharmacokinetics, Journal of Pharmaceutical Investigation 48(1) (2018) 43-60.
[3] A. Shah, M.A. Dobrovolskaia, Immunological effects of iron oxide nanoparticles and iron-based complex drug formulations: Therapeutic benefits, toxicity, mechanistic insights, and translational considerations, Nanomedicine-Nanotechnology Biology and Medicine 14(3) (2018) 977-990.
[4] G. Hannon, M.A. Tutty, A. Prina-Mello, Immunotoxicity and Safety Considerations for Iron Oxide Nanoparticles, in: N.T.K. Thanh (Ed.), Clinical Applications of Magnetic Nanoparticles: Design to Diagnosis Manufacturing to Medicine, CRC Press - Taylor & Francis Group, Boca Raton, FL, USA, 2018, pp. 273-287.
[5] G. Hannon, J. Lysaght, N.J. Liptrott, A. Prina-Mello, Immunotoxicity Considerations for Next Generation Cancer Nanomedicines, Advanced Science 6(19) (2019).
[6] FDA, Medical Devices Cleared or Approved by FDA in 2018, 2018. https://www.fda.gov/medical-devices/recently-approved-devices/2018-device-approvals. (Accessed Nov 2019).
[7] S. Hua, M.B.C. de Matos, J.M. Metselaar, G. Storm, Current Trends and Challenges in the Clinical Translation of Nanoparticulate Nanomedicines: Pathways for Translational Development and Commercialization, Frontiers in Pharmacology 9 (2018).
[8] Q. Dai, S. Wilhelm, D. Ding, A.M. Syed, S. Sindhwani, Y.W. Zhang, Y.Y. Chen, P. MacMillan, W.C.W. Chan, Quantifying the Ligand-Coated Nanoparticle Delivery to Cancer Cells in Solid Tumors, Acs Nano 12(8) (2018) 8423-8435.
[9] S. Wilhelm, A.J. Tavares, Q. Dai, S. Ohta, J. Audet, H.F. Dvorak, W.C.W. Chan, Analysis of nanoparticle delivery to tumours, Nature Reviews Materials 1(5) (2016).
[10] W.S. Xie, Z.H. Guo, F. Gao, Q. Gao, D. Wang, B.S. Liaw, Q. Cai, X.D. Sun, X.M. Wang, L.Y. Zhao, Shape-, size- and structure-controlled synthesis and biocompatibility of iron oxide nanoparticles for magnetic theranostics, Theranostics 8(12) (2018) 3284-3307.
[11] M.X. Jiao, P.S. Zhang, J.L. Meng, Y.Y. Li, C.Y. Liu, X.L. Luo, M.Y. Gao, Recent advancements in biocompatible inorganic nanoparticles towards biomedical applications, Biomaterials Science 6(4) (2018) 726-745.
[12] M.M. Xie, Y.L. Xu, J. Huang, Y.C. Li, L.Y. Wang, L.L. Yang, H. Mao, Going even smaller: Engineering sub-5 nm nanoparticles for improved delivery, biocompatibility, and functionality, Wiley Interdisciplinary Reviews-Nanomedicine and Nanobiotechnology.
[13] M. Amiri, M. Salavati-Niasari, A. Akbari, Magnetic nanocarriers: Evolution of spinel ferrites for medical applications, Advances in Colloid and Interface Science 265 (2019) 29-44.
[14] J.B. Schlenoff, Zwitteration: Coating Surfaces with Zwitterionic Functionality to Reduce Nonspecific Adsorption, Langmuir 30(32) (2014) 9625-9636.
[15] K.P. Garcia, K. Zarschler, L. Barbaro, J.A. Barreto, W. O'Malley, L. Spiccia, H. Stephan, B. Graham, Zwitterionic-Coated "Stealth" Nanoparticles for Biomedical Applications: Recent Advances in Countering Biomolecular Corona Formation and Uptake by the Mononuclear Phagocyte System, Small 10(13) (2014) 2516-2529.
[16] Z.J. Xiong, M.W. Shen, X.Y. Shi, Zwitterionic Modification of Nanomaterials for Improved Diagnosis of Cancer Cells, Bioconjugate Chemistry 30(10) (2019) 2519-2527.
[17] A.C.G. Weiss, H.G. Kelly, M. Faria, Q.A. Besford, A.K. Wheatley, C.S. Ang, E.J. Crampin, F. Caruso, S.J. Kent, Link between Low-Fouling and Stealth: A Whole Blood

Biomolecular Corona and Cellular Association Analysis on Nanoengineered Particles, Acs Nano 13(5) (2019) 4980-4991.
[18] L.L. Rouhana, J.A. Jaber, J.B. Schlenoff, Aggregation-Resistant Water-Soluble Gold Nanoparticles, Langmuir 23(26) (2007) 12799-12801.
[19] H.S. Choi, W. Liu, P. Misra, E. Tanaka, J.P. Zimmer, B.I. Ipe, M.G. Bawendi, J.V. Frangioni, Renal clearance of quantum dots, Nature Biotechnology 25(10) (2007) 1165-1170.
[20] W. Xiao, J. Lin, M. Li, Y. Ma, Y. Chen, C. Zhang, D. Li, H. Gu, Prolonged in vivo circulation time by zwitterionic modification of magnetite nanoparticles for blood pool contrast agents, Contrast Media & Molecular Imaging 7(3) (2012) 320-327.
[21] H. Wei, N. Insin, J. Lee, H.S. Han, J.M. Cordero, W.H. Liu, M.G. Bawendi, Compact Zwitterion-Coated Iron Oxide Nanoparticles for Biological Applications, Nano Letters 12(1) (2012) 22-25.
[22] H. Wei, O.T. Bruns, O. Chen, M.G. Bawendi, Compact zwitterion-coated iron oxide nanoparticles for in vitro and in vivo imaging, Integrative Biology 5(1) (2013) 108-114.
[23] S. Mondini, M. Leonzino, C. Drago, A.M. Ferretti, S. Usseglio, D. Maggioni, P. Tornese, B. Chini, A. Ponti, Zwitterion-Coated Iron Oxide Nanoparticles: Surface Chemistry and Intracellular Uptake by Hepatocarcinoma (HepG2) Cells, Langmuir 31(26) (2015) 7381-7390.
[24] K. Pombo-García, S. Weiss, K. Zarschler, C.-S. Ang, R. Hübner, J. Pufe, S. Meister, J. Seidel, J. Pietzsch, L. Spiccia, H. Stephan, B. Graham, Zwitterionic Polymer-Coated Ultrasmall Superparamagnetic Iron Oxide Nanoparticles with Low Protein Interaction and High Biocompatibility, ChemNanoMat 2(10) (2016) 959-971.
[25] C. Qiao, J. Yang, L. Chen, J. Weng, X. Zhang, Intracellular accumulation and immunological responses of lipid modified magnetic iron nanoparticles in mouse antigen processing cells, Biomaterials Science 5(8) (2017) 1603-1611.
[26] B.H. Kim, N. Lee, H. Kim, K. An, Y.I. Park, Y. Choi, K. Shin, Y. Lee, S.G. Kwon, H.B. Na, J.G. Park, T.Y. Ahn, Y.W. Kim, W.K. Moon, S.H. Choi, T. Hyeon, Large-Scale Synthesis of Uniform and Extremely Small-Sized Iron Oxide Nanoparticles for High-Resolution T-1 Magnetic Resonance Imaging Contrast Agents, Journal of the American Chemical Society 133(32) (2011) 12624-12631.
[27] C.M. Beddoes, C.P. Case, W.H. Briscoe, Understanding nanoparticle cellular entry: A physicochemical perspective, Advances in Colloid and Interface Science 218 (2015) 48-68.
[28] D. Boraschi, P. Italiani, R. Palomba, P. Decuzzi, A. Duschl, B. Fadeel, S.M. Moghimi, Nanoparticles and innate immunity: new perspectives on host defence, Seminars in Immunology 34(C) (2017) 33-51.
[29] J. Szebeni, D. Simberg, A. Gonzalez-Fernandez, Y. Barenholz, M.A. Dobrovolskaia, Roadmap and strategy for overcoming infusion reactions to nanomedicines, Nature Nanotechnology 13(12) (2018) 1100-1108.
[30] R. van der Meel, E. Sulheim, Y. Shi, F. Kiessling, W.J.M. Mulder, T. Lammers, Smart cancer nanomedicine, Nature Nanotechnology 14(11) (2019) 1007-1017.
[31] A. Henn, S. Lund, M. Hedtjarn, A. Schrattenholz, P. Porzgen, M. Leist, The Suitability of BV2 Cells as Alternative Model System for Primary Microglia Cultures or for Animal Experiments Examining Brain Inflammation, Altex-Alternativen Zu Tierexperimenten 26(2) (2009) 83-94.
[32] A.K.A. Silva, N. Luciani, F. Gazeau, K. Aubertin, S. Bonneau, C. Chauvierre, D. Letourneur, C. Wilhelm, Combining magnetic nanoparticles with cell derived microvesicles for drug loading and targeting, Nanomedicine: Nanotechnology, Biology and Medicine 11(3) (2015) 645-655.

[33] J. Bourquin, D. Septiadi, D. Vanhecke, S. Balog, L. Steinmetz, M. Spuch-Calvar, P. Taladriz-Blanco, A. Petri-Fink, B. Rothen-Rutishauser, Reduction of Nanoparticle Load in Cells by Mitosis but Not Exocytosis, Acs Nano 13(7) (2019) 7759-7770.
[34] P. Grodzinski, M. Kircher, M. Goldberg, A. Gabizon, Integrating Nanotechnology into Cancer Care, Acs Nano 13(7) (2019) 7370-7376.
[35] B.J. Du, M.X. Yu, J. Zheng, Transport and interactions of nanoparticles in the kidneys, Nature Reviews Materials 3(10) (2018) 358-374.
[36] P. Calcagnile, D. Fragouli, I.S. Bayer, G.C. Anyfantis, L. Martiradonna, P.D. Cozzoli, R. Cingolani, A. Athanassiou, Magnetically Driven Floating Foams for the Removal of Oil Contaminants from Water, Acs Nano 6(6) (2012) 5413-5419.
[37] H.Y. Zhu, S. Zhang, Y.X. Huang, L.H. Wu, S.H. Sun, Monodisperse $M_xFe_{3-x}O_4$ (M = Fe, Cu, Co, Mn) Nanoparticles and Their Electrocatalysis for Oxygen Reduction Reaction, Nano Letters 13(6) (2013) 2947-2951.
[38] S. Mondini, A.M. Ferretti, A. Puglisi, A. Ponti, PEBBLES and PEBBLEJUGGLER: software for accurate, unbiased, and fast measurement and analysis of nanoparticle morphology from transmission electron microscopy (TEM) micrographs, Nanoscale 4(17) (2012) 5356-5372.
[39] R.F. Egerton, Electron Energy-Loss Spectroscopy in the Electron Microscope, 3rd ed., Springer, New York, NY, USA, 2011.
[40] I.T. Lucas, S. Durand-Vidal, E. Dubois, J. Chevalet, P. Turq, Surface charge density of maghemite nanoparticles: Role of electrostatics in the proton exchange, Journal of Physical Chemistry C 111(50) (2007) 18568-18576.
[41] S.W. Provencher, A Constrained Regularization Method for Inverting Data Represented by Linear Algebraic or Integral-Equations, Computer Physics Communications 27 (1982) 213-227.
[42] S.W. Provencher, CONTIN - A General-Purpose Constrained Regularization Program for Inverting Noisy Linear Algebraic and
Integral-Equations, Computer Physics Communications 27 (1982) 229-242.
[43] C.L. Epstein, J. Schotland, The bad truth about Laplace's transform, Siam Review 50(3) (2008) 504-520.
[44] E. Blasi, R. Barluzzi, V. Bocchini, R. Mazzolla, F. Bistoni, IMMORTALIZATION OF MURINE MICROGLIAL CELLS BY A V-RAF/V-MYC CARRYING RETROVIRUS, Journal of Neuroimmunology 27(2-3) (1990) 229-237.
[45] F. Drago, M. Lombardi, I. Prada, M. Gabrielli, P. Joshi, D. Cojoc, J. Franck, I. Fournier, J. Vizioli, C. Verderio, ATP Modifies the Proteome of Extracellular Vesicles Released by Microglia and Influences Their Action on Astrocytes, Front Pharmacol 8 (2017) 910.
[46] W.J. Conover, Practical Nonparametric Statistics, Wiley, Hoboken, NJ, USA, 1999.
[47] Y. Benjamini, Y. Hochberg, Controlling the False Discovery Rate - A Practical and Powerful Approach to Multiple Testing, Journal of the Royal Statistical Society Series B-Statistical Methodology 57(1) (1995) 289-300.
[48] Y. Li, P. Italiani, E. Casals, N. Tran, V.F. Puntes, D. Boraschi, Optimising the use of commercial LAL assays for the analysis of endotoxin contamination in metal colloids and metal oxide nanoparticles, Nanotoxicology 9(4) (2015) 462-73.
[49] A.J. Puren, P. Razeghi, G. Fantuzzi, C.A. Dinarello, Interleukin-18 enhances lipopolysaccharide-induced interferon-gamma production in human whole blood cultures, J Infect Dis 178(6) (1998) 1830-4.
[50] M.W. Pfaffl, A new mathematical model for relative quantification in real-time RT-PCR, Nucleic Acids Res 29(9) (2001) e45.

[51] B. Fadeel, L. Farcal, B. Hardy, S. Vazquez-Campos, D. Hristozov, A. Marcomini, I. Lynch, E. Valsami-Jones, H. Alenius, K. Savolainen, Advanced tools for the safety assessment of nanomaterials, Nature Nanotechnology 13(7) (2018) 537-543.
[52] H. Wei, O.T. Bruns, M.G. Kaul, E.C. Hansen, M. Barch, A. Wisniowska, O. Chen, Y. Chen, N. Li, S. Okada, J.M. Cordero, M. Heine, C.T. Farrar, D.M. Montana, G. Adam, H. Ittrich, A. Jasanoff, P. Nielsen, M.G. Bawendi, Exceedingly small iron oxide nanoparticles as positive MRI contrast agents, Proceedings of the National Academy of Sciences of the United States of America 114(9) (2017) 2325-2330.
[53] L. Nilsson, D. Lof, B. Bergenstahl, Phenolic Acid Nanoparticle Formation in Iron-Containing Aqueous Solutions, Journal of Agricultural and Food Chemistry 56(23) (2008) 11453-11457.
[54] L. Hu, C. de Montferrand, Y. Lalatonne, L. Motte, A. Brioude, Effect of Cobalt Doping Concentration on the Crystalline Structure and Magnetic Properties of Monodisperse $Co_xFe_{3-x}O_4$ Nanoparticles within Nonpolar and Aqueous Solvents, Journal of Physical Chemistry C 116(7) (2012) 4349-4355.
[55] S. Richard, A. Saric, M. Boucher, C. Slomianny, F. Geffroy, S. Meriaux, Y. Lalatonne, P.X. Petit, L. Motte, Antioxidative Theranostic Iron Oxide Nanoparticles toward Brain Tumors Imaging and ROS Production, Acs Chemical Biology 11(10) (2016) 2812-2819.
[56] C.J. Xu, K.M. Xu, H.W. Gu, R.K. Zheng, H. Liu, X.X. Zhang, Z.H. Guo, B. Xu, Dopamine as a robust anchor to immobilize functional molecules on the iron oxide shell of magnetic nanoparticles, Journal of the American Chemical Society 126(32) (2004) 9938-9939.
[57] E. Amstad, T. Gillich, I. Bilecka, M. Textor, E. Reimhult, Ultrastable Iron Oxide Nanoparticle Colloidal Suspensions Using Dispersants with Catechol-Derived Anchor Groups, Nano Letters 9(12) (2009) 4042-4048.
[58] E. Drinkel, F.D. Souza, H.D. Fiedler, F. Nome, The chameleon effect in zwitterionic micelles: Binding of anions and cations and use as nanoparticle stabilizing agents, Current Opinion in Colloid & Interface Science 18(1) (2013) 26-34.
[59] G. Schmitz, pH of sodium acetate solutions, Journal of Chemical Education 79(1) (2002) 29-29.
[60] S.K. Mishra, B.S.H. Kumar, S. Khushu, R.P. Tripathi, G. Gangenahalli, Increased transverse relaxivity in ultrasmall superparamagnetic iron oxide nanoparticles used as MRI contrast agent for biomedical imaging, Contrast Media & Molecular Imaging 11(5) (2016) 350-361.
[61] Z.J. Zhou, L.R. Wang, X.Q. Chi, J.F. Bao, L.J. Yang, W.X. Zhao, Z. Chen, X.M. Wang, X.Y. Chen, J.H. Gao, Engineered Iron-Oxide-Based Nanoparticles as Enhanced T-1 Contrast Agents for Efficient Tumor Imaging, Acs Nano 7(4) (2013) 3287-3296.
[62] Y. Bao, J.A. Sherwood, Z. Sun, Magnetic iron oxide nanoparticles as T_1 contrast agents for magnetic resonance imaging, Journal of materials Chemistry C 6 (2018) 1280-1290.
[63] C. Verderio, L. Muzio, E. Turola, A. Bergami, L. Novellino, F. Ruffini, L. Riganti, I. Corradini, M. Francolini, L. Garzetti, C. Maiorino, F. Servida, A. Vercelli, M. Rocca, D. Dalla Libera, V. Martinelli, G. Comi, G. Martino, M. Matteoli, R. Furlan, Myeloid microvesicles are a marker and therapeutic target for neuroinflammation, Ann Neurol 72(4) (2012) 610-24.
[64] J. Priller, A. Flugel, T. Wehner, M. Boentert, C.A. Haas, M. Prinz, F. Fernandez-Klett, K. Prass, I. Bechmann, B.A. de Boer, M. Frotscher, G.W. Kreutzberg, D.A. Persons, U. Dirnagl, Targeting gene-modified hematopoietic cells to the central nervous system: use of green fluorescent protein uncovers microglial engraftment, Nat Med 7(12) (2001) 1356-61.

[65] H.J. Gao, W.D. Shi, L.B. Freund, Mechanics of receptor-mediated endocytosis, Proceedings of the National Academy of Sciences of the United States of America 102(27) (2005) 9469-9474.
[66] S.L. Zhang, J. Li, G. Lykotrafitis, G. Bao, S. Suresh, Size-Dependent Endocytosis of Nanoparticles, Advanced Materials 21(4) (2009) 419-+.
[67] E.M. Luther, C. Petters, F. Bulcke, A. Kaltz, K. Thiel, U. Bickmeyer, R. Dringen, Endocytotic uptake of iron oxide nanoparticles by cultured brain microglial cells, Acta Biomaterialia 9(9) (2013) 8454-8465.
[68] C. Petters, K. Thiel, R. Dringen, Lysosomal iron liberation is responsible for the vulnerability of brain microglial cells to iron oxide nanoparticles: comparison with neurons and astrocytes, Nanotoxicology 10(3) (2016) 332-342.
[69] R. Weissleder, M. Nahrendorf, M.J. Pittet, Imaging macrophages with nanoparticles, Nature Materials 13(2) (2014) 125-138.
[70] G.J. Oostingh, E. Casals, P. Italiani, R. Colognato, R. Stritzinger, J. Ponti, T. Pfaller, Y. Kohl, D. Ooms, F. Favilli, H. Leppens, D. Lucchesi, F. Rossi, I. Nelissen, H. Thielecke, V.F. Puntes, A. Duschl, D. Boraschi, Problems and challenges in the development and validation of human cell-based assays to determine nanoparticle-induced immunomodulatory effects, Part Fibre Toxicol 8(1) (2011) 8.
[71] Y. Li, P. Italiani, E. Casals, D. Valkenborg, I. Mertens, G. Baggerman, I. Nelissen, V.F. Puntes, D. Boraschi, Assessing the Immunosafety of Engineered Nanoparticles with a Novel in Vitro Model Based on Human Primary Monocytes, ACS Appl Mater Interfaces 8(42) (2016) 28437-28447.
[72] Y. Li, D. Boraschi, Endotoxin contamination: a key element in the interpretation of nanosafety studies, Nanomedicine (Lond) 11(3) (2016) 269-87.
[73] H. Vallhov, J. Qin, S.M. Johansson, N. Ahlborg, M.A. Muhammed, A. Scheynius, S. Gabrielsson, The importance of an endotoxin-free environment during the production of nanoparticles used in medical applications, Nano Lett 6(8) (2006) 1682-6.
[74] R. Kikkert, E.R. de Groot, L.A. Aarden, Cytokine induction by pyrogens: comparison of whole blood, mononuclear cells, and TLR-transfectants, J Immunol Methods 336(1) (2008) 45-55.
[75] FDA, CDER, CBER, CMV, CDRH, ORA, Guidance for Industry. Pyrogen and Endotoxins Testing: Questions and Answers, U.S. Food and Drug Administration, Silver Spring, MD, USA, 2012.
[76] Q. Weng, X. Hu, J. Zheng, F. Xia, N. Wang, H. Liao, Y. Liu, D. Kim, J. Liu, F. Li, Q. He, B. Yang, C. Chen, T. Hyeon, D. Ling, Toxicological Risk Assessments of Iron Oxide Nanocluster- and Gadolinium-Based T1MRI Contrast Agents in Renal Failure Rats, ACS Nano 13(6) (2019) 6801-6812.
[77] Y. Maezawa, D. Cina, S.E. Quaggin, Glomerular Cell Biology, in: R.J. Alpern, O.W. Moe, M. Caplan (Eds.), Seldin and Giebisch's The Kidney, Academic Press, San Diego, CA, USA, 2013.
[78] G. Giebisch, E. Windhager, Glomerular Filtration and Renal Blood Flow, in: W.F. Boron, E.L. Boulpaep (Eds.), Medical Physiology, Saunders Elsevire, Philadelphia, PA, USA, 2017.
[79] D. Venturoli, B. Rippe, Ficoll and dextran vs. globular proteins as probes for testing glomerular permselectivity: effects of molecular size, shape, charge, and deformability, American Journal of Physiology-Renal Physiology 288(4) (2005) F605-F613.
[80] W.L. Rice, A.N. Van Hoek, T.G. Paunescu, C. Huynh, B. Goetze, B. Singh, L. Scipioni, L.A. Stern, D. Brown, High Resolution Helium Ion Scanning Microscopy of the Rat Kidney, Plos One 8(3) (2013).

[81] R.A. Fenton, J. Praetorius, Anatomy of the Kidney, in: K. Skorecki, G.M. Chertow, P.A. Marsden, M.W. Taal, A.S.L. Yu (Eds.), Brenner and Rector's The Kidney2015.
[82] J. Rostgaard, K. Qvortrup, Electron microscopic demonstrations of filamentous molecular sieve plugs in capillary fenestrae, Microvascular Research 53(1) (1997) 1-13.
[83] K.P. Arkill, C. Knupp, C.C. Michel, C.R. Neal, K. Qvortrup, J. Rostgaard, J.M. Squire, Similar Endothelial Glycocalyx Structures in Microvessels from a Range of Mammalian Tissues: Evidence for a Common Filtering Mechanism?, Biophysical Journal 101(5) (2011) 1046-1056.
[84] I. Shirato, Y. Tomino, H. Koide, T. Sakai, Fine-structure of the glomerular-basement-membrane of the rat-kidney visualized by high-resolution scanning electron-microscopy, Cell and Tissue Research 266(1) (1991) 1-10.
[85] T. Burghardt, F. Hochapfel, B. Salecker, C. Meese, H.J. Grone, R. Rachel, G. Wanner, M.P. Krahn, R. Witzgall, Advanced electron microscopic techniques provide a deeper insight into the peculiar features of podocytes, American Journal of Physiology-Renal Physiology 309(12) (2015) F1082-F1089.
[86] F. Grahammer, C. Wigge, C. Schell, O. Kretz, J. Patrakka, S. Schneider, M. Klose, S.J. Arnold, A. Habermann, R. Brauniger, M.M. Rinschen, L. Volker, A. Bregenzer, D. Rubbenstroth, M. Boerries, D. Kerjaschki, J.H. Miner, G. Walz, T. Benzing, A. Fornoni, A.S. Frangakis, T.B. Huber, A flexible, multilayered protein scaffold maintains the slit in between glomerular podocytes, Jci Insight 1(9) (2016).
[87] E. Gagliardini, S. Conti, A. Benigni, G. Remuzzi, A. Remuzzi, Imaging of the Porous Ultrastructure of the Glomerular Epithelial Filtration Slit, Journal of the American Society of Nephrology 21(12) (2010) 2081-2089.
[88] E. Frohlich, The role of surface charge in cellular uptake and cytotoxicity of medical nanoparticles, International Journal of Nanomedicine 7 (2012) 5577-5591.
[89] N. Lee, T. Hyeon, Designed synthesis of uniformly sized iron oxide nanoparticles for efficient magnetic resonance imaging contrast agents, Chemical Society Reviews 41(7) (2012) 2575-2589.
[90] A.E. Deatsch, B.A. Evans, Heating efficiency in magnetic nanoparticle hyperthermia, Journal of Magnetism and Magnetic Materials 354 (2014) 163-172.
[91] J.H. Kang, E. Um, A. Diaz, H. Driscoll, M.J. Rodas, K. Domansky, A.L. Watters, M. Super, H.A. Stone, D.E. Ingber, Optimization of Pathogen Capture in Flowing Fluids with Magnetic Nanoparticles, Small 11(42) (2015) 5657-5666.
[92] P. Italiani, D. Boraschi, Induction of Innate Immune Memory by Engineered Nanoparticles: A Hypothesis That May Become True, Frontiers in Immunology 8 (2017).
[93] K.M. Tsoi, S.A. MacParland, X.Z. Ma, V.N. Spetzler, J. Echeverri, B. Ouyang, S.M. Fadel, E.A. Sykes, N. Goldaracena, J.M. Kaths, J.B. Conneely, B.A. Alman, M. Selzner, M.A. Ostrowski, O.A. Adeyi, A. Zilman, I.D. McGilvray, W.C.W. Chan, Mechanism of hard-nanomaterial clearance by the liver, Nature Materials 15(11) (2016) 1212-1221.
[94] B.H. Yin, K.H.K. Li, L.W.C. Ho, C.K.W. Chan, C.H.J. Choi, Toward Understanding in Vivo Sequestration of Nanoparticles at the Molecular Level, Acs Nano 12(3) (2018) 2088-2093.